Nonequilibrium dynamics of suppression, revival, and loss of charge order in a laser-pumped electron-phonon system

Sankha Subhra Bakshi,[1] Debraj Bose,[1] Arijit Dutta,[2] and Pinaki Majumdar[1]
[1]*Harish-Chandra Research Institute (A CI of Homi Bhabha National Institute), Chhatnag Road, Jhusi, Allahabad 211019, India*
[2]*Institut für Theoretische Physik, Goethe-Universität, 60438 Frankfurt am Main, Germany*

(Received 14 May 2024; revised 12 July 2024; accepted 17 July 2024; published 1 August 2024)

An electron-phonon system at commensurate filling often displays charge order (CO) in the ground state. Such a system subject to a laser pulse shows a wide variety of behavior. A weak pulse sets up low-amplitude oscillations in the order parameter, with slow decay to a slightly suppressed value. A strong pulse leads to destruction of the charge order with the order parameter showing rapid, oscillatory, decay to zero. The regime in-between, separating the weak pulse CO sustained state from the strong pulse CO destroyed state, shows an initial rapid decay of the order parameter, followed by a low-amplitude quiescent state, and the rise to a finite steady-state value over a timescale τ_{cr}. The steady-state value goes to zero and τ_{cr} diverges as the pulse amplitude is increased towards a critical strength. We provide a complete characterization of the dynamics in this nonequilibrium problem for varying electron-phonon coupling and pulse strength, highlight the multiple gap-closing and -opening transitions that occur, and suggest a simple dynamical model incorporating the pulse-induced nonequilibrium electron population.

DOI: 10.1103/PhysRevB.110.075102

I. INTRODUCTION

Recent experiments have started to explore the quantum dynamics in correlated electron systems [1–20]. The method involves imparting energy to the electron system via an electromagnetic pulse and studying the evolution by probing time dependence of the photoemission spectra or optical conductivity [21–26]. Although all experimental systems are in some thermal environment, at short enough time the pulse-driven systems probe quantum states at energies much higher than what temperature alone would allow. To that extent one probes "athermal" dynamics. The excess energy imparted by the pulse can lead to various nonequilibrium phenomena including melting of order [3–10], the emergence of new order [11–14], and "transitions" in transport and optical behavior [8,9], all of these arising from a nonthermal population of excitations.

For systems coupled to a thermal bath, at long time the added energy is dissipated and one attains the equilibrium state, but the transient dynamics can be very interesting. For a system that is nominally thermally isolated, i.e., cannot dissipate the added energy, neither the transient nor the steady state is known *a priori*. In particular, one key question is whether the long-time state admits an equilibrium description with an effective temperature. Finally, a system that is periodically driven can display steady states which do not have an equilibrium counterpart [27–29].

Our focus is on the dynamics in a "thermally isolated" charge-ordered electron-phonon (EP) system subject to a laser pulse, and the spatiotemporal dynamics that arises as a result. One expects that as the added energy increases the charge order will be progressively suppressed, and ultimately destroyed. That is indeed the answer at long times. What is far less obvious is the dynamics associated with this process. This paper provides a real-space, real-time description of this process and suggests a phenomenology to explain the microscopic answers. Before summarizing our method and key results we touch upon what is known about the equilibrium charge-ordered state in EP systems, and what recent pump-probe experiments have revealed about dynamics.

Strong electron-phonon interaction leads to the formation of an electron-phonon bound state, the lattice polaron, which serves as the basic degree of freedom at strong coupling [30–32]. At commensurate electron filling the polarons can order into a "charge-ordered" (CO) state, involving periodic modulation of the bond lengths and electron density [33,34]. The equilibrium physics of such CO systems is well understood [35–38].

Recent experimental advances allow strong perturbation of the CO state by application of a laser pulse (the "pump") and probe the resulting electron-phonon dynamics via time- and angle-resolved photoemission spectroscopy (trARPES) [17,22–24] or resonant inelastic x-ray scattering (RIXS) [25,26]. The pump adds excess energy to the electrons which, due to the presence of EP interaction, get transferred in part to the lattice. As a result, suppression and eventually melting of charge order can be observed. Such experiments have been done on 1T-TaS_2 [10], tritellurides [18], and the cuprates [26] in their charge-ordered phases. Depending on the strength of the photoexcitation the following features are observed. (i) Weak photoexcitation leads to a damped periodic modulation of the electronic gap as well as the electronic temperature [18,26]. (ii) With increasing photoexcitation one sees dynamics where the charge order vanishes at short times and then recovers slowly to a suppressed value. This is accompanied by an insulator-metal-insulator transition as a function of time

[15,16]. (iii) At strong photoexcitation the CO melts rapidly, resulting in an insulator-metal (I-M) transition [19,20].

The dynamics in response to a weak pump pulse can be understood via linear response theory [39,40], as also the system's response to a probe pulse [41–43]. However, the strongly perturbed system displays dynamics that require the solution of the full time-dependent problem. For this, one can employ a phenomenological time-dependent Ginzburg-Landau theory [44,45], or fully microscopic approaches.

The microscopic difficulty is in handling widely different electron and phonon timescales at strong coupling. For EP systems methods like exact diagonalization (ED) [46] and dynamical mean field theory (DMFT) [47,48] provide accurate results on electronic timescales but cannot access the real-space correlations. ED calculations are severely limited by system size.

Given the energy-scale difference between electrons and phonons in the adiabatic regime, and the related need to retain a large tower of phonon states, the approach could be to treat the phonons classically. This approach has been used within a Monte Carlo scheme recently to explain the ringing in the EP system on photoexcitation [49]. The method still requires iterative diagonalization to evolve the system and for a large system size diagonalization even for "noninteracting" electrons become too costly to capture the rich dynamics of the order parameter. Our method, below, allows access to "long times" at modest computational cost and captures all the key features of order-parameter dynamics in a charge-ordered system.

We use a "mean field dynamics" (MFD) scheme to study the dynamics of the CO state in the half-filled (spinless) Holstein model in two dimensions. We set up coupled equations of motion for the expectation values of the phonon displacement operator $\hat{x}_i(t)$ and the electron bilinear $\hat{\rho}_{ij}(t) = c_i^\dagger(t)c_j(t)$. The equations close when one factorizes the electron-phonon interaction term. The computation is an $O(N^2)$ process for each time step and the number of time steps required range from 10^6 to 10^8. Despite its apparent simplicity the method captures the effect of strong EP coupling and spatial correlations accurately. It goes beyond the "static phonon" (or adiabatic) approximation, widely used before [50]. An approach similar to ours has been used recently to study the double-exchange model [51].

We work at intermediate EP coupling (below the single-polaron threshold) and probe the pulse strength (E_0) dependence of the dynamics. Our primary indicators are the phonon amplitude at the ordering wave vector $x_{\mathbf{Q}}(t)$ and the charge density wave field $n_{\mathbf{Q}}(t)$, where $\mathbf{Q} = (\pi/a_0, \pi/a_0)$ on our square lattice with spacing a_0. We set $a_0 = 1$. Our main results are the following:

(1) *Long-time state.* With increasing pulse amplitude E_0 the long-time state attained by the system changes from charge ordered to charge disordered at a critical amplitude E_0^c. At the EP coupling where we study the problem E_0^c also demarcates a gap-closing transition in the long-time electronic state.

(2) *Transient response.* There are three regimes in terms of pulse strength: (i) For $E_0 \ll E_0^c$ the indicators $|x_{\mathbf{Q}}|$ and $|n_{\mathbf{Q}}|$ show oscillatory decay towards a suppressed long-time value. (ii) For $E_0 \to E_0^c$, these indicators first show a drop towards zero over a timescale of few phonon oscillations, remain small for a time $\tau_{\rm cr}$, and then rise towards a finite steady-state value. (iii) For $E_0 > E_0^c$, the indicators decay monotonically to zero.

(3) *"Critical" slowing down.* For $E_0 \to E_0^c$ from below, $|x_{\mathbf{Q}}(t \to \infty)|^2$ and $|n_{\mathbf{Q}}(t \to \infty)|^2$ vanish as $(E_0^c - E_0)^\alpha$ where $\alpha \sim 0.7$. We find that $\tau_{\rm cr}$ diverge as $(E_0^c - E_0)^{-\nu}$, where $\nu \sim 0.45$.

(4) *Time-dependent spectrum.* Constructing a density of states (DOS) from the instantaneous eigenvalues we find that the DOS remains gapped at all times when $E_0 \ll E_0^c$, and ungapped at all times for $E_0 > E_0^c$. For $E_0 \to E_0^c$ the DOS first shows gap closing and then reopening as a function of time.

(5) *Phenomenology.* The coupled dynamics of electrons and phonons can be approximated by the dynamics of the phonons in the presence of a force arising from a *nonequilibrium* electron population. Parametrizing this population distribution based on the full dynamics and using a Langevin equation allows us to capture both the suppression-revival dynamics as well as the "critical behavior."

This paper is organized as follows. In Sec. II we define the model, explain the dynamical scheme, and set out the parameter space. In Sec. III we classify and study the different regimes in order-parameter dynamics. In Sec. IV we examine the dynamics of the overall system, including the time dependence of the energy distribution over momentum modes, the electronic density of states, and the population of "excited" electrons. Based on these we construct an effective classical model for the phonon dynamics in Sec. V, allowing access to large spatial scales and long times. Section VI discusses issues related to our analytic and numerical approximations and Sec. VII concludes the paper.

II. MODEL AND METHOD

A. Model and evolution equation

The Holstein model is given by

$$\begin{aligned} H &= H_e + H_{\rm ph} + H_{ep} \\ &= \sum_{ij} t_{ij}\hat{c}_i^\dagger \hat{c}_j + \sum_i \left(\frac{\hat{p}_i^2}{2M} + \frac{K\hat{x}_i^2}{2}\right) - g\sum_i \hat{n}_i\hat{x}_i. \end{aligned} \quad (1)$$

For the t_{ij} we consider nearest-neighbor hopping on a square lattice. M is the phonon mass, K the stiffness, and g the electron-phonon coupling.

We start by writing the Heisenberg equation for $\hat{x}_i$, leading to the family below. Setting $\hbar = 1$,

$$\begin{aligned} \frac{d\hat{x}_i}{dt} &= -i[\hat{x}_i, H] = \frac{\hat{p}_i}{M}, \\ \frac{d\hat{p}_i}{dt} &= -i[\hat{p}_i, H] = -K\hat{x}_i + g\hat{n}_i. \end{aligned} \quad (2)$$

Now there are different options. (i) One can take an average on the left- and right-hand sides of the equations and replace $\langle\hat{n}_i(t)\rangle$ by its expectation in the instantaneous phonon background $x_i(t)$. This is the "adiabatic evolution" scheme, and involves iterative diagonalization of the electron problem in "classical" phonon backgrounds $\{x_i\}$ to compute the force on the phonons. Alternately, (ii) one can go beyond the adiabatic scheme and write an equation of motion for the $\hat{n}_i(t)$ itself, and so on, and close the hierarchy at some order. Following

this route, for our $\hat{\rho}_{ij}(t) = c_i^\dagger(t)c_j(t)$,

$$\frac{d\hat{\rho}_{ij}}{dt} = -i[\hat{\rho}_{ij}, H] = -i\left[\hat{\rho}_{ij}, \sum_{mn}\hat{h}_{nm}\hat{\rho}_{mn}\right], \tag{3}$$

where $\hat{\rho}_{ij} = c_i^\dagger c_j$ and $\hat{h}_{ji} = t_{ij} - g\hat{x}_i\delta_{ij}$. Using $[c_\alpha^\dagger c_\beta, c_m^\dagger c_n] = \delta_{m\beta}c_\alpha^\dagger c_n - \delta_{n\alpha}c_m^\dagger c_\beta$ and simplifying the commutators, we obtain

$$\begin{aligned}\frac{d\hat{\rho}_{ij}}{dt} &= -i\sum_k(\hat{\rho}_{ik}\hat{h}_{kj} - \hat{h}_{ik}\hat{\rho}_{kj}) \\ &= -i\sum_k(\hat{\rho}_{ik}t_{jk} - \hat{\rho}_{kj}t_{ki}) + ig(\hat{x}_i - \hat{x}_j)\hat{\rho}_{ij}. \end{aligned}\tag{4}$$

The first term on the right-hand side comes purely from the hopping, the second term, however, involves a coupling between electron and phonon variables. The equations are not closed and now we need to know the dynamics of mixed objects like $\hat{x}_i\hat{\rho}_{ij}$. This leads to the Bogoliubov-Born-Green-Kirkwood-Yvon (BBGKY) hierarchy. We truncate the hierarchy by taking the expectation value of the left- and right-hand sides and approximating $\langle\hat{x}_i\hat{\rho}_{jk}\rangle \approx \langle\hat{x}_i\rangle\langle\hat{\rho}_{jk}\rangle$. For notational simplicity we define the expectation value of an operator as $\langle\hat{O}\rangle = O$. The factorization leads to a closed family of equations.

This "nonadiabatic evolution" scheme involves two processes: (i) the phonons are "driven" by $-Kx_i + gn_i$, with $n_i = \rho_{ii}$, where ρ is the one-body "density operator" and (ii) the density operator ρ_{ij} is nonlocally correlated and driven by the x_j. The coupled equations that we get from this are

$$\begin{aligned} M\frac{d^2x_i}{dt^2} &= -Kx_i + g\rho_{ii}, \\ \frac{d\rho_{ij}}{dt} &= -i\sum_k(\rho_{ik}h_{kj} - h_{ik}\rho_{kj}) \\ \text{with}\quad h_{ij} &= t_{ji} - x_j\delta_{ji}. \end{aligned}\tag{5}$$

On a lattice with N sites, there are N values of x_i and N^2 elements in the matrix ρ_{ij}. We have to solve $N^2 + 2N$ first-order (in time) nonlinear differential equations.

B. Generating the initial configuration

We consider the equilibrium system to be in its ground state. At half-filling $n = 0.5$, the Holstein model with nearest-neighbor hopping has a charge-ordered ground state at all g. We obtain the reference CO state by minimizing the total energy with respect to a periodic x_i field. At the minimum, $\{x_i^0\}$, say, we use the the eigenvectors of $H\{x_i^0\}$ to compute the averages $\rho_{ij}^0 = \langle c_i^\dagger c_j\rangle_0$.

C. Modeling the laser pulse

We include the laser field via Peierls substituion. This leads to the time-dependent hopping term

$$H_e(t) = \sum_{ij} t_{ij}\left(e^{i\int_{\vec{r}_j}^{\vec{r}_i}\vec{A}(t)\cdot\vec{dr}}c_i^\dagger c_j + \text{H.c.}\right), \tag{6}$$

$$\vec{E}(t) = -\frac{d\vec{A}(t)}{dt} = \vec{E}_0\exp\left[-\left(\frac{t-t_0}{\tau_p}\right)^2\right]\cos(\Omega_p t). \tag{7}$$

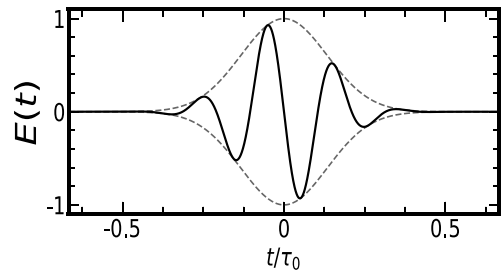

FIG. 1. Laser pulse parameters: We set the pulse width to $\tau_p = \tau_0/10$, the pulse frequency $\Omega_p = 5\Omega_0$, and vary the magnitude of the electric field E_0 from 0.01–1.0. We plot the time dependence of the electric field, normalized by E_0.

E_0 is the strength of the field, τ_p and the Ω_p are the width of the pulse and frequency of the incident wave, respectively. The electric field is taken in $(\vec{x} + \vec{y})$ direction. We set $t_0 = 0$. The time dependence of the electric field associated with the laser pulse is shown in Fig. 1.

D. Parameter space

In the rest of the paper we will use t as the time variable and denote the hopping t_{ij} as $-t_{\text{hop}}$ for nearest neighbors, and set $t_{\text{hop}} = 1$. We set $K = 1$ and the oscillator mass to $M = 25$ so that the local phonon frequency is $\Omega_0 = \sqrt{K/M} = 0.2$. As a result the "adiabaticity" parameter $\gamma = \Omega_0/t_{\text{hop}} = 0.2$ is small but not negligible. We measure time in units of $\tau_0 = 2\pi/\Omega_0$. We focus on the half-filled case $n = 0.5$. In the adiabatic regime the energy of a polaron is $E_p \sim -g^2/2K$. A polaron forms when this equals the band bottom energy $-4t_{\text{hop}}$ (in two dimensions). This leads to the definition of a dimensionless EP coupling strength: $\lambda = g^2/8Kt_{\text{hop}}$. Single-polaron formation, in the adiabatic limit, corresponds to $\lambda \sim 1$. In this paper we work mainly with $\lambda = 0.38$, intermediate coupling, but well below the single-polaron threshold. We set $\Omega_p/\Omega_0 = 5$ and $\tau_p = \tau_0/10$. Having fixed n, t_{hop}, Ω_0, λ, and the pulse parameters τ_p and Ω_p, we study the response of the half-filled CO state to a laser pulse for varying pulse amplitude E_0.

E. Numerical techniques

Most of our data are on system size $N = 16 \times 16$. We use the Runge-Kutta 4 (RK4) method to solve $N^2 + 2N$ coupled first-order differential equations for x_i, p_i, and ρ_{ij}. Our step parameter is set to $\delta t = \tau_0/1500$ and our total run length τ_{max} is at least $6000\tau_0$. In the critical pulse regime, where the system undergoes a transition from the CO state to a charge-disordered state, simulation timescales needed to access the steady state grow rapidly. There we have used $\tau_{\text{max}} \sim 10^5\tau_0$ (on system size 12×12).

F. Indicators

Our basic output is the time series for $x_i(t)$. Based on this we can compute various correlation functions of the phonon variables. We can compute the instantaneous electronic density of states (DOS) from the electronic eigenvalues ϵ_n in a background $x_i(t)$. We also have access to the equal-time corre-

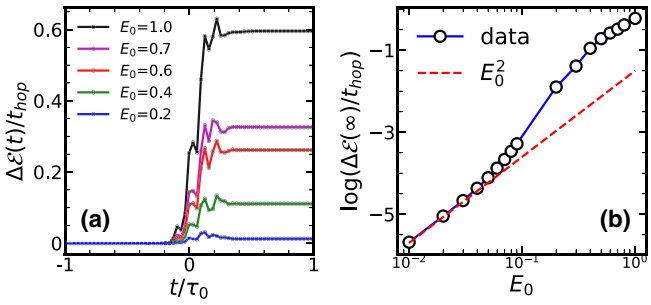

FIG. 2. (a) The time dependence of the added energy energy $\Delta\mathcal{E}(t)$. The energy of the unperturbed system is $\mathcal{E}(0)$ and pumping injects additional energy into the system. Since the postpulse dynamics is conservative, the total energy $\mathcal{E}(t) = \mathcal{E}(0) + \Delta\mathcal{E}(t)$ should be constant for $t \gg \tau_p$. The panel confirms this and also quantifies the added energy. (b) The dependence of $\Delta\mathcal{E}(\infty)$ on E_0, showing the "linear response" regime $\Delta\mathcal{E}(\infty) \propto E_0^2$ and beyond.

lation $\rho_{ij}(t) = \langle c_i^\dagger(t) c_j(t)\rangle$ and can compute the "occupation" of levels $\epsilon_n(t)$ from this.

The spatial Fourier transforms related to phonon distortions and density are, respectively,

$$x_{\mathbf{q}}(t) = \frac{1}{N}\sum_{ij} e^{i\mathbf{q}\cdot\mathbf{r}_i} x_i(t), \quad n_{\mathbf{q}}(t) = \frac{1}{N}\sum_{ij} e^{i\mathbf{q}\cdot\mathbf{r}_i} n_i(t), \tag{8}$$

where $n_i(t) = \rho_{ii}(t)$. There are the corresponding Fourier transforms to frequency of the fluctuations:

$$\delta x_{\mathbf{q}}(\omega) = \int_0^{t_{\max}} dt\, e^{-i\omega t}[x_{\mathbf{q}}(t) - \bar{x}_{\mathbf{q}}],$$
$$\bar{x}_{\mathbf{q}} = \frac{1}{t_{\max}}\int_0^{t_{\max}} dt\, x_{\mathbf{q}}(t) \tag{9}$$

and the same for $\delta n_{\mathbf{q}}(\omega)$.

We also calculate the following instantaneous distributions:

$$P(x,t) = \frac{1}{N}\sum_i \delta[x - x_i(t)],$$
$$N(\omega,t) = \frac{1}{N}\sum_n \delta[\omega - \epsilon_n(t)],$$
$$f(\omega,t)N(\omega,t) = \sum_n \rho_{nn}(t)\delta[\omega - \epsilon_n(t)]. \tag{10}$$

$P(x,t)$ is the distribution of lattice distortions, $N(\omega,t)$ is the electronic density of states, and $f(\omega,t)$ the electronic occupation of the instantaneous eigenstates. ρ_{nn} is the expectation value of the density operator associated with the nth eigenstate with energy ϵ_n: $\rho_{nn}(t) = \sum_{ij} U^*_{in}(t) U_{jn}(t)\rho_{ij}(t)$, where $U(t)$ are the instantaneous eigenvectors.

In the absence of an external drive, our method of evolution strictly conserves the energy. If the prepulse energy of the system is $\mathcal{E}(0)$ and the pump-induced change is $\Delta\mathcal{E}$ then $\mathcal{E}(t) = \mathcal{E}(0) + \Delta\mathcal{E}(t)$. We find that for $t \gg \tau_p$, $\Delta\mathcal{E}(t)$ becomes a constant, which we call $\Delta\mathcal{E}(\infty)$. In Fig. 2(a) we depict the time evolution of $\mathcal{E}(t)$ for varying E_0. Figure 2(b) shows the energy absorbed $\Delta\mathcal{E}(\infty)$ against E_0, revealing that at low E_0, it is proportional to E_0^2 as expected from linear response.

III. DYNAMICS OF THE ORDER PARAMETER

A. Overall behavior

Before entering into the detailed characterization of the dynamics we attempt a broad classification of regimes that occur for varying E_0. Figure 3 illustrates the different dynamical regimes that arise in response to pulses of increasing strength. The data are for $\lambda = 0.38$, and the results have a similar trend at other λ. The charge-ordered state corresponds to $O(1)$ value of the Fourier transform $x_{\mathbf{Q}} = (1/N)\sum_i x_i e^{i\mathbf{Q}\cdot\mathbf{r}_i}$, the order parameter of the CO state. Figure 3 shows the time dependence of $|x_{\mathbf{Q}}(t)|$. The prepulse value is normalized to 1 for convenience.

Figures 3(a) and 3(b) are in the "weak pulse" regime where we mainly see oscillatory decay to a long-time value that is suppressed with respect to the prepulse (equilibrium) value. We will call this response "weak oscillatory suppression" (WOS).

At very weak pulse strength one expects weakly damped oscillation of the various normal modes of the CO state. The oscillation frequency would be $\Omega^0_{\mathbf{q}}$, the electronically renormalized phonon dispersion about the CO state. The amplitude of oscillation of the modes will depend on the specific nature of the perturbation. The order-parameter mode will have a response of the form $x_{\mathbf{Q}} \sim A + B\cos(\Omega^0_{\mathbf{Q}} t)$. As the pulse strength increases, a mode coupling induced damping, and associated decay time, will emerge. We call this τ_w, and the associated, pulse renormalized, oscillation frequency as $\Omega_{\mathbf{Q}}$. Note that "weak" in our nomenclature refers to the overall weak suppression of $x_{\mathbf{Q}}$. It does not correspond to a weak perturbation regime in terms of linear response.

Figure 3(c) show results in the critical pulse regime where $|x_{\mathbf{Q}}(t)|$ initially drops almost to zero, stays there for some time, and then "revives" heading towards a finite long-time value. We call this "strong suppression and revival" (SSR) dynamics. Ignoring the sharp drop at small times, the longer-time behavior can be described roughly by $x_{\mathbf{Q}}(t) \sim Ae^{-(\tau_{cr}/t)^\beta} + B\cos(\Omega_{\mathbf{Q}} t)$. The "waiting time" in the low-amplitude state is decided by $\sim\tau_{cr}$, while the approach to the long-time state has a power-law character $1 - (\tau_{cr}/t)^\beta$.

Figure 3(d) shows $|x_{\mathbf{Q}}(t)|$ in the strong pulse regime where we see a monotonic decay of the oscillation envelope to zero and there is no revival. This is simply "monotonic suppression" (MS) dynamics. A simple analytic form for $x_{\mathbf{Q}}(t)$ is $A(1 - e^{-(\tau_s/t)^\gamma})\cos(\Omega_{\mathbf{Q}} t)$.

We collect together the suggested expressions for $x_{\mathbf{Q}}(t)$:

$$x_{\mathbf{Q}}(t) \sim A + Be^{-t/\tau_w}\cos(\Omega_{\mathbf{Q}} t) \quad \text{(weak)}$$
$$\sim Ae^{-(\tau_{cr}/t)^\beta} + B\cos(\Omega_{\mathbf{Q}} t) \quad \text{(critical)}$$
$$\sim A(1 - e^{-(\tau_s/t)^\gamma})\cos(\Omega_{\mathbf{Q}} t) \quad \text{(strong)}. \tag{11}$$

In this paper, the function $x_{\mathbf{Q}}(t)$ is fitted, but $|x_{\mathbf{Q}}(t)|$ is plotted to emphasize the dynamics of the magnitude.

Figure 4 shows the global phase diagram in the λ-E_0 plane, highlighting both the long-time state and the dynamical regimes. It is based on analysis of the kind shown in Fig. 3,

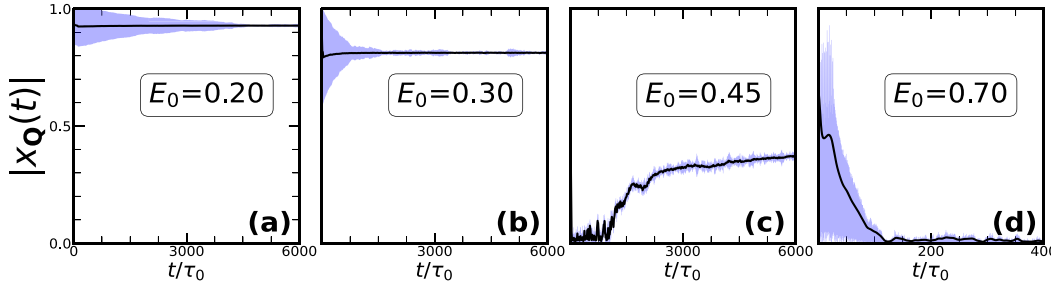

FIG. 3. Overview of dynamics of the order-parameter mode $|x_{\mathbf{Q}}|$ for different E_0. Upper row: (a)–(d) Show real-time dynamics $|x_{\mathbf{Q}}(t)|$. (a), (b) Weak pulse regime, roughly $E_0 = 0 - 0.35$, where $x_{\mathbf{Q}}(t)$ oscillates with a single frequency and decays to a suppressed CO state. (c) Critical pulse regime, roughly $E_0 = 0.35$–0.50, where $x_{\mathbf{Q}}(t)$ is rapidly suppressed, stays small for a time window, and then rises to a low-amplitude long-time state. (d) Strong pulse regime $E_0 > 0.5$, where the CO gets destroyed within a few τ_0 while the phonon ringing continues for a longer time. The black line corresponds to the "mean curve" plotted by averaging $|x_{\mathbf{Q}}(t)|$ within $10\tau_0$.

now carried out for several λ. The blue region corresponds to surviving CO, while the red region corresponds to a state with CO destroyed in response to the pulse. In the ordered region, dark blue corresponds to the weak oscillatory suppression (WOS) defined earlier, while light blue corresponds to strong suppression and revival (SSR). Red region is charge disordered, where the dynamics is of monotonic suppression (MS), and is separated from the ordered regime by the nonequilibrium phase transition. A true phase transition, with $|x_{\mathbf{Q}}(t \to \infty)| \to 0$, as E_0 tends to some E_0^c, can be seen only as $L \to \infty$ and $t_{\max} \to \infty$. The boundary in Fig. 4 is drawn via extrapolation of L-dependent data at a few sizes, 12×12 to 20×20.

B. Weak pulse regime

Figure 5 shows in detail the phonon and charge density dynamics at the ordering wave vector $\mathbf{Q}$ for a pulse with $E_0 = 0.30$. For the density field there is an initial drop, on the scale of a few τ_0. This is followed by an oscillatory decay to a long-time state for both phonon and density field. Figures 5(a) and 5(c) show $|x_{\mathbf{Q}}|$ and $|n_{\mathbf{Q}}|$, respectively, over the whole run, while the insets show the time dependence at short times

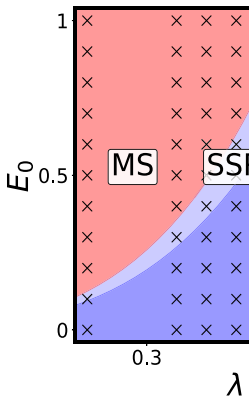

FIG. 4. λ-E_0 global phase diagram in terms of the long-time state and the dynamics that arises in response to a pulse. In the blue regions the long-time state has charge order. In dark blue (WOS), $|x_{\mathbf{Q}}|$ shows an oscillatory decay towards its long-time CO state. In region light blue (SSR), $|x_{\mathbf{Q}}|$ shows an initial decay to zero and then revives towards a low-amplitude CO state at long times. In red region (MS), $|x_{\mathbf{Q}}|$ shows monotonic decay to zero with no revival. The boundary between regions blue and red is a phase transition. The "cross" marks represent the available data points.

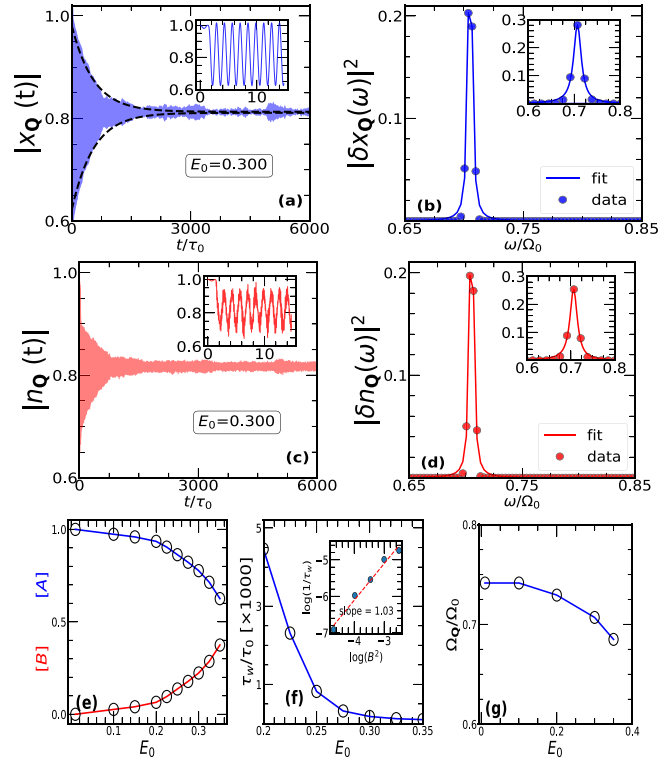

FIG. 5. Weak pulse regime: (a) Shows $|x_{\mathbf{Q}}(t)|$ with the inset highlighting the very short-time behavior. Dotted line in (a) shows the fit of the envelope with the fitting function discussed in the text. (b) Shows $|\delta x_{\mathbf{Q}}(\omega)|^2$, obtained by Fourier transform over the entire time window, while the inset shows the transform of data over the interval $t \sim [0$–$15]\tau_0$. (c), (d) Show corresponding data for $|n_{\mathbf{Q}}(t)|$ and $|\delta n_{\mathbf{Q}}(\omega)|^2$. Note the quick drop in $|n_{\mathbf{Q}}(t)|$ at very short time. (e) Shows the amplitude $A(E_0)$, with A being the steady-state value of $|x_{\mathbf{Q}}(t)|$ at the ordering wave vector $\mathbf{Q}$. (f) Shows the timescale τ_w over which the main oscillations decay. It diverges as $E_0 \to 0$ when the dynamics reduces to decoupled normal modes. In the inset we plot $\log(B^2)$ with $\log(\tau_w^{-1})$, which suggests $\tau_w^{-1} \sim 1/B^2$. (g) Shows the oscillation frequency $\Omega_{\mathbf{Q}}$.

$\sim 15\tau_0$. As we have argued, $x_{\mathbf{Q}}(t) \sim A + Be^{-t/\tau_w}\cos(\Omega_{\mathbf{Q}}t)$. This simple function does not capture the oscillations (and the "beating pattern") at $t \gg \tau_w$ but seems adequate for an overall description. Also, to capture the $t = 0$ state we should have $A + B = 1$. Figures 5(b) and 5(d) show the respective Fourier transforms of their fluctuations, the main panel showing the transform of the full time series and the inset showing the transform of the short-time response. We fit the $|x_{\mathbf{Q}}|$ envelope using the fitting function defined earlier. According to the fitting function, the $t \to \infty$ value of $|x_{\mathbf{Q}}|$ is A and there will be a peak in the spectrum around $\Omega_{\mathbf{Q}}$ with width τ_w^{-1}. Figure 5(e) shows the E_0 dependence of A and B. A falls from 1 at $E_0 = 0$ to $\sim$0.6 at $E_0 \sim 0.35$ while B rises from zero to about 0.4.

Figure 5(f) shows $\tau_w(E_0)$, which has a remarkable decrease with increasing E_0. As $E_0 \to 0$ the weakly perturbed lattice has only undamped normal mode oscillations, and $\tau_w \to \infty$. Since τ_w^{-1} emerges from anharmonicity, in the weak pulse limit we expect it to vary as a power B^{α}. A plot of log(B) versus $\log(\tau_w^{-1})$ suggests that $\tau_w^{-1} \sim B^2$.

The oscillation frequency $\Omega_{\mathbf{Q}}$ shows only weak E_0 dependence as shown in Fig. 5(g). The frequency for low-amplitude oscillations on the CO state is given by $\Omega_{\mathbf{Q}}^0 = \sqrt{\Omega_0^2 - (g^2/m)\Pi_{\mathbf{Q}}^0}$, where $g^2\Pi_0(\mathbf{q})$ is the lowest-order phonon self-energy [52]. Specifically, it is the static limit of the frequency-dependent self-energy $g^2\Pi_0(\mathbf{q}, \Omega)$, where

$$\Pi_0(\mathbf{q}, \Omega) = \left[\frac{1}{N\beta}\sum_{\mathbf{k},n} G_{\mathbf{k}}^{\omega_n} G_{\mathbf{k}+\mathbf{q}}^{\omega_n+\Omega_m}\right]_{i\Omega_m \to \Omega + i\eta, \eta \to 0}, \quad (12)$$

where $G_{\mathbf{k}}(i\omega_n)$ is the electronic Green's function in the perfect CO state. Electron-phonon coupling gives a dispersion to the phonons, and also lowers the frequency from the bare value Ω_0. The effect of the added energy due to E_0 is to additionally reduce $\Omega_{\mathbf{Q}}$, akin to what one observes in the effect of temperature [53].

C. Critical pulse strength regime

For $E_0 \gtrsim 0.35$ the nature of $|x_{\mathbf{Q}}(t)|$ changes. Beyond a few cycles of oscillatory response both the phonon and charge density fields are suppressed to roughly $\sim$1%–2% of their prepulse value, and persist in this state, with small oscillations, for a timescale that we call $\tau_{\rm cr}$. Beyond this both $|x_{\mathbf{Q}}(t)|$ and $|n_{\mathbf{Q}}(t)|$ "revive," reaching a finite but low-amplitude long-time state. Figures 6(a) and 6(c) show the time dependence of the two structure factors at $E_0 = 0.45$, the main panels show the overall time dependence, while the inset shows the initial drop that occurs over $\sim 25\tau_0$. A description of the form $x_{\mathbf{Q}}(t) \sim Ae^{-(\tau_{\rm cr}/t)^{\beta}} + B\cos(\Omega_{\mathbf{Q}}t)$ captures multiple features of the complex dynamics. Beyond the initial drop the function above captures the following features of the data: (i) The low-amplitude quiescent state, at $t \lesssim \tau_{\rm cr}$, is described by exponentially small contribution from the first term, and small oscillations $B|\cos(\Omega_{\mathbf{Q}}t)|$, with $B \ll 1$. (ii) As t goes beyond $\tau_{\rm cr}$ the A term makes a significant contribution, seen in the rise of the mean curve. The exponential saturates for $t \gg \tau_{\rm cr}$ but long-term oscillations persist. (iii) Finally, the mean value of $|x_{\mathbf{Q}}|$ rises as $1 - (\tau_{cr}/t)^{\beta}$ at long times, a power law rather than exponential rise to the steady state.

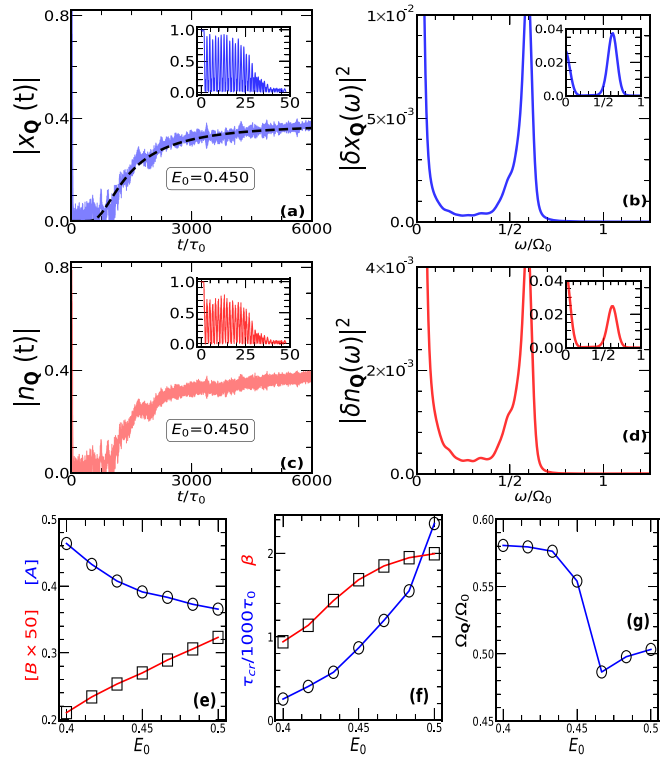

FIG. 6. Critical pulse strength regime: (a), (c) Show behavior of $|x_{\mathbf{Q}}(t)|$ and $|n_{\mathbf{Q}}(t)|$, respectively. Dotted line in (a) shows the fit of the envelope with the fitting function discussed in text. Corresponding insets show the behavior at short times $t \lesssim 50\tau_0$. At short time the order in both phonons and electrons decays to zero. Then there is a very low-amplitude quiescent state, followed by a "revival," rising to the long-time value as $\sim e^{-(\tau/t)^{\beta}}$. The respective line shapes (b) and (d) show a peak near zero as well as broad finite-frequency feature at $\Omega_{\mathbf{Q}}$. (e)–(g) Fitting parameters for $x_{\mathbf{Q}}(t)$. (e) The amplitude A (blue) that decides the steady-state value of $|x_{\mathbf{Q}}|$ and B (red) that decides the size of oscillations. Note $B \ll A$. (f) The increase in $\tau_{\rm cr}$ (blue) by more than an order of magnitude while E_0 varies only from 0.41 to 0.47, and the exponent β (red) which stays between 0–1. (g) The frequency $\Omega_{\mathbf{Q}}$ shows nonmonotonic behavior in E_0.

Figures 6(b) and 6(d) show $|\delta x_{\mathbf{Q}}(\omega)|^2$ and $|\delta n_{\mathbf{Q}}(\omega)|^2$, respectively. There are the usual features around $\Omega_{\mathbf{Q}}$. There is also a low-energy feature, whose peak location and width are $\sim(\tau_{\rm max} - \tau_{\rm cr})^{-1}$, as we have checked through numerical transform of our model function.

As we have stated the single scale $\tau_{\rm cr}$ describes both the low-amplitude quiescent state as well as the power-law rise to the steady state. Figure 6(e) shows the amplitudes $A(E_0)$ and $B(E_0)$. In a later figure we will show the size dependence of this result, allowing us to extract the critical behavior. Figure 6(f) shows the rapid rise of the "delay time" $\tau_{\rm cr}$ that is needed for revival of the CO state. It also shows the exponent β that controls the power-law approach to the steady state. Figure 6(g) shows the primary frequency $\Omega_{\mathbf{Q}}$.

D. Strong pulse regime

Figure 7 shows the detailed dynamics at $E_0 = 1.0$, which is in the strong pulse regime. Figure 7(a) shows $|x_{\mathbf{Q}}(t)|$: it has

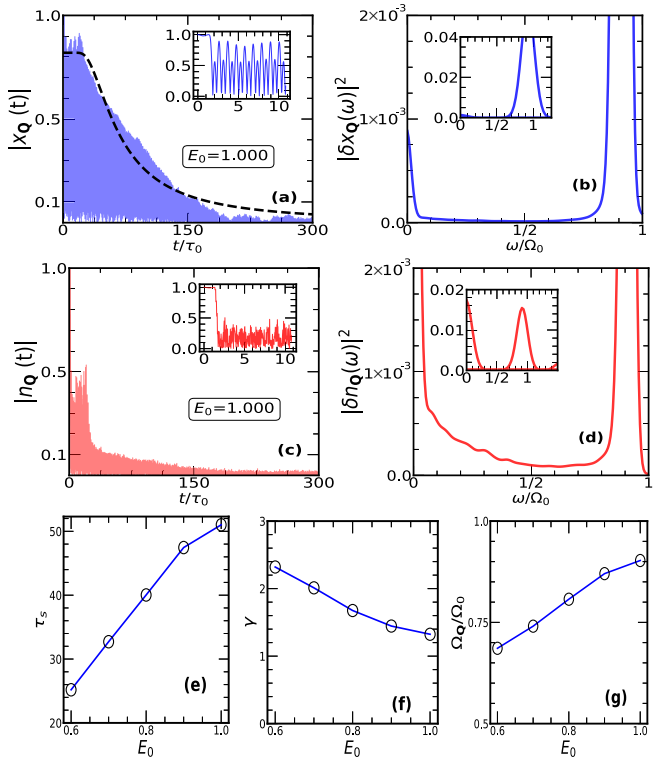

FIG. 7. Strong pulse regime: (a) The relatively slow decay of $|x_{\mathbf{Q}}(t)|$ contrasted with (c) the rapid suppression of $|n_{\mathbf{Q}}(t)|$. Dotted line in (a) shows the fit of the envelope with the fitting function discussed in text. (b), (d) Show the Fourier transforms of the fluctuations of $x_{\mathbf{Q}}(t)$ and $n_{\mathbf{Q}}(t)$, respectively. (e), (f) Shows monotonic increase of τ_s and decrease of the exponent γ with E_0. (g) Shows the increase in the oscillation frequency towards Ω_0 as E_0 increases. We are not showing the amplitude A, which stays almost constant at $A \sim 0.88$.

a modest drop on the scale of τ_0, then a period of roughly constant amplitude oscillation for about $25\tau_0$, and finally a decay to zero that seems to be fit by a power law. For our fitting function $x_{\mathbf{Q}}(t) \sim A(1 - e^{-(\tau_s/t)^{\gamma}})\cos(\Omega_{\mathbf{Q}}t)$, the $t \ll \tau_s$ regime is of fixed amplitude oscillation $|A\cos(\Omega_{\mathbf{Q}}t)|$ while for $t \gg \tau_s$ we get a behavior $|A(\tau_s/t)^{\gamma}\cos(\Omega_{\mathbf{Q}}t)|$.

The response in the charge sector Fig. 7(c)] is very different. $|n_{\mathbf{Q}}|$ falls sharply from 1 to ∼0.15 within $t \sim \tau_0$, then has roughly fixed amplitude oscillations for $t \lesssim \tau_s$, and then abruptly collapses. We do not see any prominent power-law tail (at least at this value of E_0) unlike in $|x_{\mathbf{Q}}|$. Figures 7(b) and 7(d) show the corresponding Fourier transforms of their fluctuations. Both of these have the usual peaks at $\Omega_{\mathbf{Q}}$.

Figure 7(e) shows the timescale τ_s obtained from the fitting. This *increases* initially with increasing E_0 (past E_0^c) and then tends to saturate. Figure 7(f) shows the exponent γ, which reduces from ∼2.5 to ∼1.5 as E_0 increases from 0.6 to 1.0. In (g) $\Omega_{\mathbf{Q}}$ increases with E_0 tending to the bare Ω_0 (independent local oscillators) at large E_0. The amplitude A is almost flat in this regime at $A = 0.88$.

IV. DYNAMICS OF THE OVERALL SYSTEM

Until now the focus has been on the order-parameter mode at $\mathbf{q} = (\pi, \pi) \equiv \mathbf{Q}$. We now pay attention to the other $\mathbf{q}$ modes to which energy is transferred from $\mathbf{Q}$ via mode coupling, and also the electron population, which dictates the overall energy sharing between electrons and phonons.

A. Dynamics of momentum modes

We first look at evolution of $|x_{\mathbf{q}}(t)|^2$ over the Brillouin zone (BZ) for three representative values of pulse amplitude. We also examine $|\delta x_{\mathbf{q}}(\omega)|^2$, obtained by Fourier transforming the fluctuations of $x_{\mathbf{q}}(t)$ over the whole time window, for scans across the BZ.

Our $x_i(t)$ is "driven" by the density variable $n_i(t)$. When the x_i and the corresponding density deviate only slightly from the ideal periodic value we obtain normal mode vibrations at frequencies given by $\Omega_{\mathbf{q}}^0 = \sqrt{\Omega_0^2 - (g^2/m)\Pi_0(\mathbf{q})}$ as described earlier.

This undamped oscillatory behavior is observed only at very weak pumping, as we have seen in Fig. 3(a). It does not capture mode coupling, that leads to damping, or to the loss and revival phenomena that we observe in the critical regime. These effects involve the energy distribution over all $\mathbf{q}$ as a function of time and also the nature of electronic excitations.

Figure 8 shows maps of $|x_{\mathbf{q}}|$ at different times for three values of E_0 and the associated $|\delta x_{\mathbf{q}}(\omega)|^2$. In the left column, at $t = 0$ (prepulse) and for all values of E_0, the only "bright" feature is at $\mathbf{q} = \mathbf{Q}$. Other modes are inactive. The principal observations from the time dependence are the following:

(i) *Weak pulse regime (top row).* At short time $\sim 50\tau_0$, the first additional features show up along the diagonal of the Brillouin zone (BZ). The peak at $\mathbf{Q}$ still remains the most prominent. At $75\tau_0$ there are more excitations along the diagonal and by $150\tau_0$ the whole BZ is "lit up" the brightest part being along the diagonal. This is related to the nature of the pump, which is along $\vec{x} + \vec{y}$ and causes an initial current in the $\vec{x} + \vec{y}$ direction. The mode at $\mathbf{Q}$ remains the most prominent at all times, diminishing slightly in intensity. The Fourier transform $|\delta x_{\mathbf{q}}(\omega)|^2$ essentially matches the phonon dispersion $\Omega_{\mathbf{q}}^0$ of the charge-ordered phase, but with the brightest intensity at $\mathbf{q} = \mathbf{Q}$.

(ii) *Critical pulse regime (middle row).* The spreading of energy over the BZ happens quickly and suppresses the peak at $\mathbf{Q}$. Until $\sim 1000\tau_0$ there is no prominent feature in the BZ. Beyond this a peak at $\mathbf{Q}$ reemerges and gains some weight. The intensity at the longest time $5000\tau_0$ is far below what it was at $t = 0$. The associated Fourier transform looks very different from the linear response $\Omega_{\mathbf{q}}$, and is actually reminiscent of what one observes in the equilibrium problem near its thermal transition.

(iii) *Strong pulse regime (bottom row).* The $x_{\mathbf{Q}}$ amplitude diminishes monotonically with time and by $\sim 100\tau_0$ there is no trace of the peak at $\mathbf{Q}$. The corresponding $|\delta x_{\mathbf{q}}(\omega)|^2$ shows an almost flat, momentum-independent, structure, with uniform distribution of amplitude across $\mathbf{q}$ similar to the equilibrium high-temperature case. The $\mathbf{q}$ space picture reveals how energy is distributed over the BZ as a function of time. It does not explain whether the destruction of CO, as in the critical and strong pulse regimes, occur due to imperfect "phase correlations" between ordered domains, or due to the destruction of charge modulations itself. That requires examination of the spatial density n_i as a function of time.

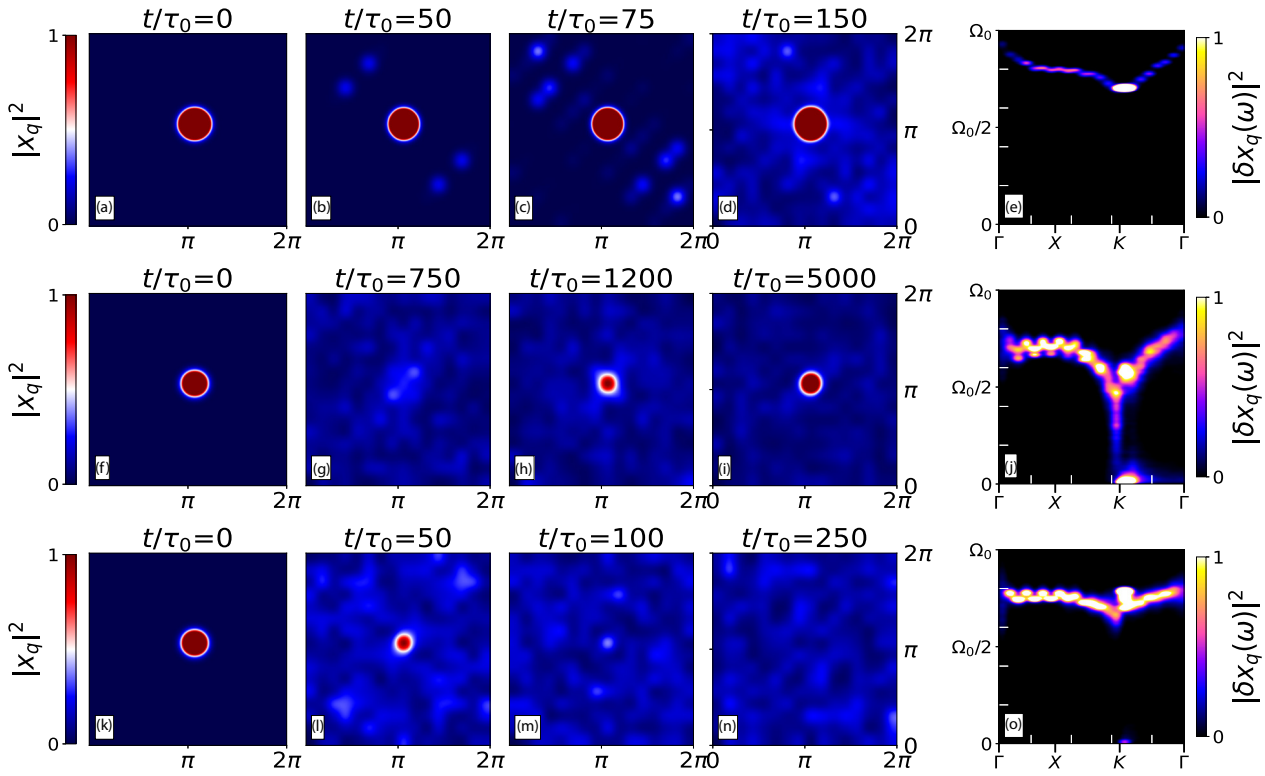

FIG. 8. The time dependence of $|x_{\mathbf{q}}|^2$ over the entire Brillouin zone (BZ), and the associated frequency dependence, in the three pulse regimes. Top row: weak pulse ($E_0 = 0.2$). (a)–(d) With increasing t first the intensity of $\mathbf{q}$ modes along the diagonal increase and finally all $\mathbf{q}$ modes become active. However the $\mathbf{q} = \mathbf{Q}$ mode retains its dominant position. (e) shows the $|\delta x_{\mathbf{q}}(\omega)|^2$, obtained via Fourier transform of $x_{\mathbf{q}}(t)$ over the whole time range, on a selected path $\Gamma(0,0) - X(\pi,0) - K(\pi,\pi) - \Gamma(0,0)$ in $\mathbf{q}$-space. The response maps out the equilibrium phonon dispersion but with weight mostly centered at K-point. Middle row: critical regime ($E_0 = 0.43$). (f)–(i) There is a quick transfer of energy to $\mathbf{q}$ modes all over the Brillouin zone (BZ) and at $t = 750\tau_0$ there is no peak at $\mathbf{q} = \mathbf{Q}$. By $1200\tau_0$ there is a recovery and by $5000\tau_0$ the intensity approaches the long time asymptote. (j) Frequency dependence reveals phonon band softening and broadening and a significant dip near K. Bottom row: strong pulse ($E_0 = 0.7$). The timescales here are shorter than in the upper rows. The mode at $\mathbf{Q}$ initially transfers energy along the diagonal of the BZ, which then cascades to the rest of the BZ. By $t \sim 100\tau_0$ the energy has been distributed almost evenly over the BZ and there is no peak at $\mathbf{q} = \mathbf{Q}$. (o) The phonon-band starts flattening again and the mean frequency increases.

B. Spatial pattern and distribution functions

Figure 9, top row, shows maps of n_i in the critical window. The main effect at intermediate time $\sim(10^2 - 10^3)\tau_0$ is the homogenization of the charge density. We can call it "amplitude disordering," in contrast to "phase disordering" where modulations remain but interference between domains suppresses order. For $t \gtrsim 1500\tau_0$ the density modulations reappear, though much weaker than before, and spatially organize. At the longest time shown the n_i field has a well-organized alternating pattern, though the modulations about $n = 0.5$ are only $\frac{1}{3}$ of the $t = 0$ value, and there is some amplitude inhomogeneity. The disordering and revival seems to be an amplitude effect rather than a domain interference effect. Phase slippage, i.e., boundaries between the two complementary charge order states CO and CO′, is not playing an important role in the delayed recovery. Rather, competition between the "metallic state" (homogeneous density) and suppressed CO is seemingly playing the crucial role.

When comparing the pump-driven decay and revival to the order-parameter growth induced by thermal quench, some differences become apparent. In the thermal situation the competition between complementary ordered phases CO and CO′ plays a more significant role. At very low temperatures, the system assumes a CO state among the two symmetry-broken states (with Z_2 symmetry). However, for $T \gtrsim T_{\mathrm{CO}}$ while locally CO patches exist the interference between domains suppresses the order parameter $x_{\mathbf{Q}}$. When the system is thermally quenched, from $T > T_{\mathrm{CO}}$ to $T < T_{\mathrm{CO}}$ it is domain growth that controls order-parameter recovery. The *magnitude* of the distortions is unaffected as long as the temperatures involved are much less than $g^2/2K$.

In the photopumped case a laser pulse quickly homogenizes the lattice distortions and the charge distribution, suppressing $x_{\mathbf{Q}}$ and $n_{\mathbf{Q}}$. The amplitude of the distortions has to grow before domains can form and compete for reconstruction of long-range order. So, if the thermal quench mainly involves "phase ordering," in the photopumped case both amplitude and phase are important. This is evident when we look at the destruction of the bimodality in the distribution function $P(n)$ discussed below.

The second row shows the distribution of densities $P(n)$ at different times. At $t = 0$, $P(n)$ shows a bimodal structure with ± 0.3 modulation around $n = 0.5$. The postpump state at $300\tau_0$ shows a single peak centered at the mean density

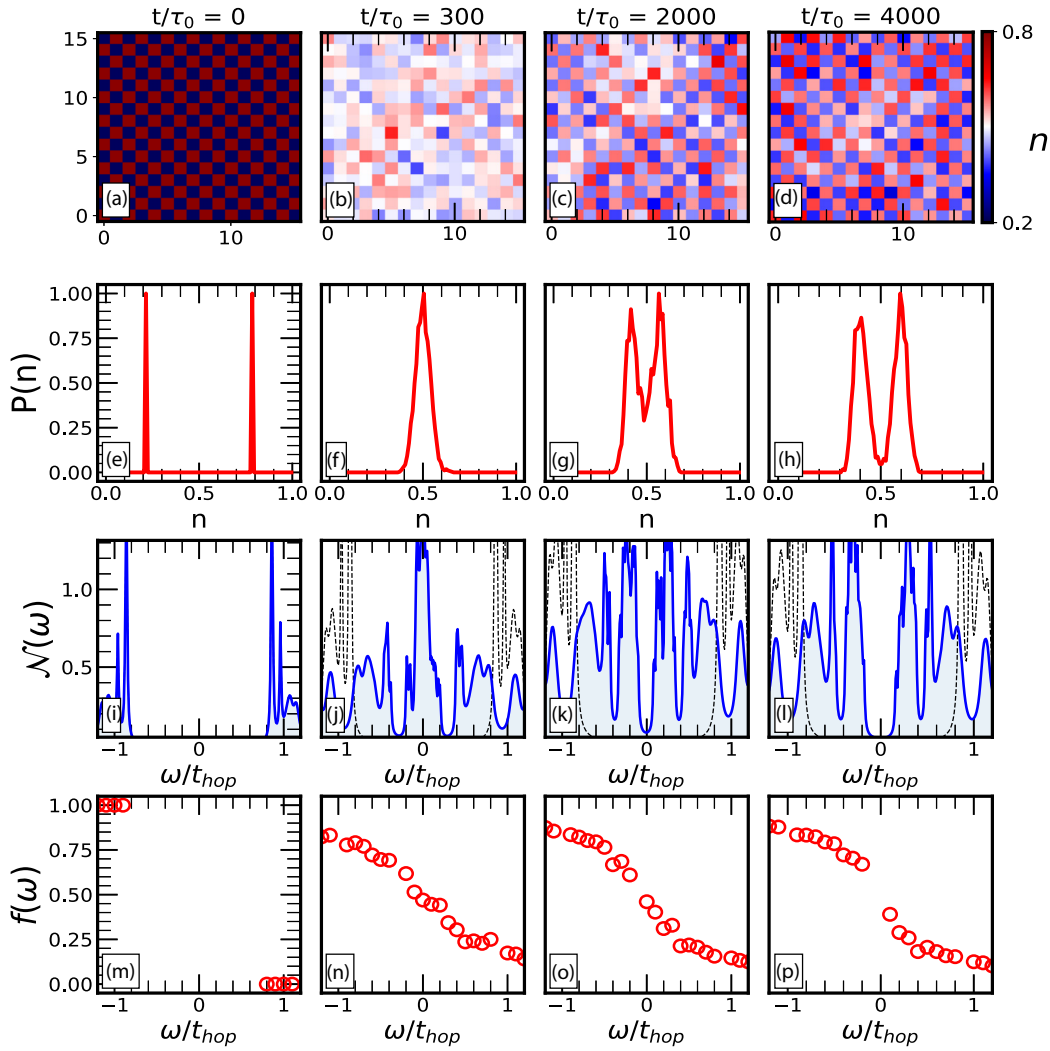

FIG. 9. Time dependence of spatial distribution and electronic properties in the critical pulse regime $E_0 = 0.45$. First row: spatial variation of electron density n_i. At $t = 0$ we have perfect checkerboard order n_i taking values ∼0.2 and 0.8 at alternate sites. Second row: the distribution of density $P(n, t)$ corresponding to the spatial maps above. The $P(n)$ is sharply bimodal. At $t = 300\tau_0$ the n_i map shows that charge modulations have essentially vanished, and $P(n)$ shows a unimodal distribution peaked around $n = 0.5$. At $t = 2000\tau_0$ we again see the reemergence of charge modulations, a checkerboard structure, and a bimodal feature in $P(n)$. The last column shows the "revived" charge density, now varying roughly between 0.4 and 0.6. This is roughly $\frac{1}{3}$ the charge modulation in the $t = 0$ state. The $P(n)$ has a clearer bimodal feature now. Third row: density of states $\mathcal{N}(\omega)$ based on the instantaneous eigenvalues in the $x_i(t)$ background. At $t = 0$ there is a gap $\sim 1.6t_{\rm hop}$. The gap closes around $\sim 300\tau_0$ and starts to reopen around $\sim 2000\tau_0$. It reaches a saturation value $\sim 0.5t_{\rm hop}$ around $\sim 4000\tau_0$. Fourth row: the occupation function $f(\omega, t)$. The prepump distribution is the zero-temperature Fermi function. The pump depletes low-energy states and creates population at significantly high energies. After the gap reopens a large upper-band population still retains.

$n = 0.5$. Around $t = 1500\tau_0$ this starts to broaden, showing a hint of bimodality, and spatial configuration shows patches of charge order (CO). At $t = 2000\tau_0$ we see a clear bimodal structure which sharpens by $4000\tau_0$.

The third row shows the instantaneous DOS at different times obtained by binning the eigenvalues $\epsilon_n(t)$ of the electronic Hamiltonian in the background $x_i(t)$. The prepump state has a gap $\sim 1.5t$. At $t \sim 300\tau_0$ the gap has vanished and the DOS shows a prominent peak at $\omega = 0$. Beyond this, with increasing t, as the lattice distortions increase and organize in the (π, π) pattern again, spectral weight is lost at low energy. At $t = 2000\tau_0$ a small gap shows up in the spectrum which grows to about $\sim\frac{1}{3}$ of the $t = 0$ value at the longest time $4000\tau_0$.

In contrast to the equilibrium state at zero temperature, where electronic occupancy is dictated by a sharp Fermi distribution, in the postpump situation the occupancy of the instantaneous eigenstates is time dependent and nonzero for $\omega > 0$ states as well. The bottom row illustrates the occupation of these levels derived from $\rho_{nn}(t)$ by projecting ρ_{ij} onto the instantaneous eigenvectors. At $t = 0$, i.e., before the pulse, it is the usual Fermi function $\theta(-\omega)$. The pump induces transitions to the upper band. By $t \gtrsim 300\tau_0$ the postpump distribution assumes a smooth form. Subsequently, as the gap begins to open around $2000\tau_0$, a significant population of excited electrons $n_{\rm exc}$ remains in the upper band. In this particular case, $n_{\rm exc}$ amounts to approximately 25%.

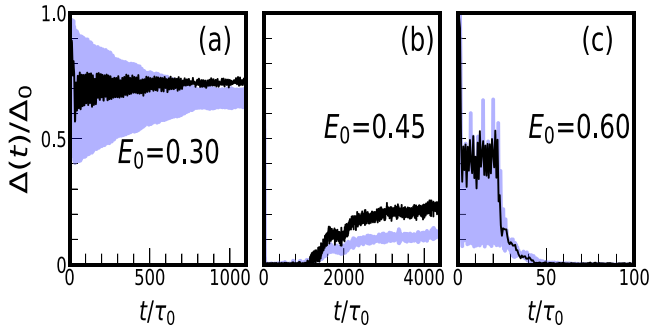

FIG. 10. Behavior of the gap in the electronic DOS (black) computed from the instantaneous spectrum at different E_0. In weak pulse regime $E_0 = 0.3$, $\Delta(t)$ oscillates then relaxes to 70% of Δ_0. In critical regime $E_0 \sim 0.45$, $\Delta(t)$ shows suppression and revival. In the strong pulse regime $E_0 = 0.6$, $\Delta(t)$ goes to zero by $\sim 50\tau_0$. $\Delta(t)$ is closely correlated with $|x_{\mathbf{Q}}(t)|^2$ (blue). Both $\Delta(t)$ and $|x_{\mathbf{Q}}(t)|^2$ were normalized by their initial equilibrium value.

Figure 10 quantifies the time dependence of the gap $\Delta(t)$ inferred from the instantaneous spectrum. In the weak pulse regime the gap $\Delta(t)$ (normalized by Δ_0) shows oscillatory behavior, followed be a relaxation to a slightly suppressed value. For example, at $E_0 \sim 0.3$ it stabilizes to $\sim$70% of its original value. In the critical regime, the instantaneous gap shows an oscillatory behavior but averaged over a $10\tau_0$ timescale (black line) it shows suppression and revival dynamics. In strong pulse regime, the gap goes to zero within $\sim 100\tau_0$. It can be noticed that this normalized gap is closely correlated with the normalized $|x_{\mathbf{Q}}(t)|^2$ as shown in the figure with faint blue line.

V. RESULTS FROM A SIMPLE CLASSICAL MODEL

Full mean field dynamics is expensive since it involves an $O(N^2)$ process for every microscopic step δt. The dynamics needs to be tracked to a time $\tau_{\max}$, that is needed to reach the asymptotic state, and $\tau_{\max}$ grows with system size.

The electron-phonon problem has a hierarchy of timescales, $\delta t \ll {t_{\rm hop}}^{-1} \ll \tau_0 \ll \tau_{\max}$. Typically $\delta t \sim 10^{-3}\tau_0$ and $\tau_{\max} \sim 10^4\tau_0$. That indicates that the $O(N^2)$ MFD update process has to be carried out $\sim 10^7$ times, limiting us to sizes $\sim 20 \times 20$. While the qualitative physics of suppression, revival, and loss of order is accessible on this spatial scale and timescale, a simpler model, with much greater spatiotemporal reach, can be motivated from the lessons in the last section.

The lessons are as follows: (i) The pump creates an "upper band" population that decays to nonzero value over a short timescale. This excited population $n_{\rm exc}$ persists over a very long time and can be approximated by a Fermi distribution with some temperature $T_{\rm el}$. (ii) The effective temperatures of the electron and phonon system are not the same, on timescales that we probe. They differ by orders of magnitude. We discuss the estimation of these $T_{\rm el}$ and $T_{\rm ph}$ from MFD in Appendix A. (iii) There is the usual growth and interference of CO domains as with any ordering phenomena. This needs to be handled in a real-space setting. All this requires a model that captures large distortion physics nonperturbatively, incorporates intersite coupling that promotes a checkerboard pattern, and a mechanism to sense the population of excited electrons.

We will model the excited electron population with a time-dependent electronic temperature $T_{\rm el}$ estimated from MFD. Since $T_{\rm el}(t)$ plays a key role in what follows, we clear up the notation. As a result of pumping, $T_{\rm el}(t)$ quickly attains a high "initial value," denoted $T_{\rm el}^i$. As electrons relax, $T_{\rm el}(t)$ decreases towards its "final" value $T_{\rm el}^f$. These initial and final values, and the rate of decrease, specified by a form $e^{-t/\tau_{\rm el}}$, completely specify $T_{\rm el}(t)$. From MFD we find that $T_{\rm el}^i/T_{\rm el}^f$ and $\tau_{\rm el}$ are roughly independent of E_0. This allows us to encode the effect of pulse strength in only one parameter $T_{\rm el}^f$. Just as values of E_0 separate different regimes within MFD, values of $T_{\rm el}^f$ will separate different regimes in the effective model we now define.

A. Constructing the model

The simplest model for large distortion induced electron trapping is one electron on two sites (one electron on one site is trivial since the hopping term is absent). For this, the electronic part of the model is

$$H_2^{\rm el} = -t_{\rm hop}(c_1^\dagger c_2 + c_2^\dagger c_1) - g(n_1 x_1 + n_2 x_2). \tag{13}$$

Treating the x as classical, the two eigenvalues of this are elementary:

$$\lambda_\pm = -\frac{g x_+}{2} \pm \sqrt{\frac{g^2 x_-^2}{4} + t_{\rm hop}^2}, \tag{14}$$

where $x_\pm = x_1 \pm x_2$ and $\mu = -g^2/2K$. If the electrons sense an effective temperature $T_{\rm el}$, that creates the upper level population, then the free energy associated with the electronic part is

$$F_{\rm el}(x_1, x_2) = -T_{\rm el} \ln(e^{-\beta_{\rm el}\lambda_-} + e^{-\beta_{\rm el}\lambda_+}). \tag{15}$$

Adding the stiffness terms, the effective "potential" dictating the dynamics of the x_i is

$$V(x_1, x_2) = \frac{K}{2}\left(x_1^2 + x_2^2\right) + F_{\rm el}(x_1, x_2). \tag{16}$$

A couple of comments before we generalize V to the lattice, i.e., construct an approximate $V(x_1, \ldots, x_N)$. (i) The potential is symmetric under the interchange of x_1 and x_2. (ii) For $T_{\rm el} \to 0$ we have $F_{\rm el} \to \lambda_-$ and minimizing with respect to x_+ and x_- leads to

$$\bar{x}_+ = \frac{g}{K}, \quad \bar{x}_- = \pm\frac{1}{g}\sqrt{\left(\frac{g^2}{K}\right)^2 - t^2}. \tag{17}$$

(iii) At large g the lowest eigenvalue can arise from two x configurations: $(x_1 = g/K,\ x_2 = 0)$ and its complement. The corresponding charge density would be (1,0) or (0,1). (iv) We will see later that as $T_{\rm el}$ increases the tendency to have a modulation x_- reduces.

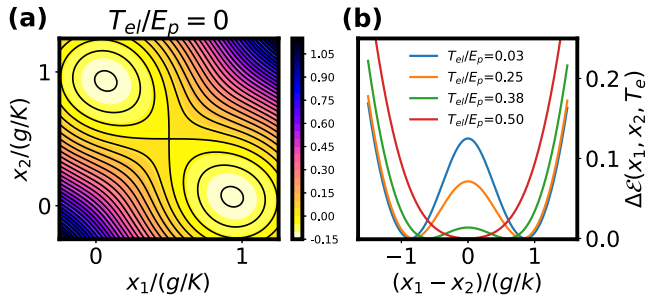

FIG. 11. (a) Effective potential $V(x_1, x_2)$ at $T_{\rm el} = 0$, and (b) the nature of $V(x_1 - x_2)$ with increasing $T_{\rm el}$.

Putting these together we propose a phonon model of the form

$$H_{\rm ph}^{\rm eff} = \sum_i \frac{p_i^2}{2M} + \frac{K}{2}\sum_i x_i^2 + \frac{1}{z}\sum_{\langle ij\rangle} V(x_i, x_j), \tag{18}$$

$$V(x_i, x_j) = -T_{\rm el}\ln(e^{-\beta_{el}\lambda_-} + e^{-\beta_{el}\lambda_+}). \tag{19}$$

Here z is the number of nearest neighbors. In two dimensions (2D), it is 4. $\lambda_\pm$ is a function of x_i, x_j. The parameters involved in $H_{\rm ph}^{\rm eff}$ are all defined already in the Holstein model, except for $T_{\rm el}$, which we extract by fitting the excited population in the full MFD to a thermal distribution (Appendix A). The MFD based $n_{\rm exc}(t, E_0)$ is mapped on to a $n_{\rm exc}(t, T_{\rm el})$. Thankfully, the time dependence of $T_{\rm el}$ is simple: it settles to its long-time value quickly and the lattice dynamics plays out in the background of this "final" electron temperature $T_{\rm el}^f$.

The effective potential for two sites can be written as $V(x_+, x_-) = V_1(x_-) + V_2(x_+)$ and, at half-filling, this assumes the form

$$V_1(x_-) = \frac{1}{4}Kx_-^2 - T_{\rm el}\ln[e^{-\beta_{\rm el}\bar{\lambda}} + e^{+\beta_{\rm el}\bar{\lambda}}], \tag{20}$$

$$V_2(x_+) = \frac{1}{4}Kx_+^2 - \frac{1}{2}gx_+, \tag{21}$$

$$\bar{\lambda}(x_-) = \sqrt{\frac{1}{4}g^2x_-^2 + t_{\rm hop}^2}. \tag{22}$$

In Fig. 11 we plot this two-site effective potential as a function of x_1 and x_2 and we get two wells around $(0,\ g/K)$ and $(g/K,\ 0)$ at $T_{\rm el} = 0$ (left). When we plot the $V(x_-)$ with $T_{\rm el}$ with $x_+ = g/K$ we see a transition from double well to a single well around $T_{\rm el}/E_p \sim 0.5$. Near this critical excitation an effective Ginzburg-Landau model can be derived with $T_{\rm el}^f$-dependent parameters (see Appendix B).

B. Scheme for dynamics

With the excited electron population specified by $T_{\rm el}$ the effective "force" driving x_i is $-Kx_i - (\partial V/\partial x_i)$. If the x_i sense a thermal environment with temperature $T_{\rm ph}$ then the equation dictating x_i dynamics would be

$$M\frac{d^2x_i}{dt^2} = -\frac{\partial H_{\rm ph}^{\rm eff}}{\partial x_i} - \gamma\frac{dx_i}{dt} + \eta_i, \tag{23}$$

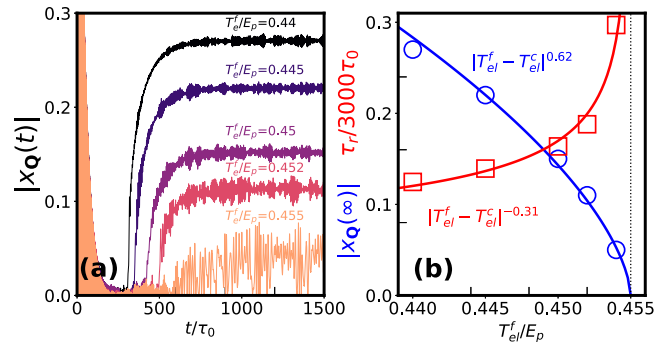

FIG. 12. In (a) the loss and revival dynamics of $|x_{\mathbf{Q}}(t)|$ with varying $T_{\rm el}^f$ is shown. (b) As $T_e^f/E_p \to 0.455$, $|x_{\mathbf{Q}}(t)| \to 0$ and recovery timescale τ_r diverges. These results are on 40×40 lattice size. We show a fit $|x_{\mathbf{Q}}| \sim |T_e^f - T_e^c|^\alpha$ near the critical regime and we find $\alpha \sim 0.62$. The τ_r shows divergence as $\tau_r \sim |T_e^f - T_e^c|^{-\nu}$ with $\nu \sim 0.31$.

where γ is a dissipation parameter and η is a white noise satisfying

$$\langle\eta_i(t)\rangle = 0, \quad \langle\eta_i(t)\eta_j(t')\rangle = 2\gamma T_{\rm ph}\delta_{ij}\delta(t - t'). \tag{24}$$

Both $T_{\rm ph}$ and γ enter in our calculations as phenomenological constants. However, we can make an estimate of these phenomenological constants from the MFD (see Appendix A). From this we get $T_{\rm ph} \sim 10^{-4}$–10^{-3} and γ is of order 10^{-2} to 10^{-1}.

C. Parameters for dynamics

The time dependence of $T_{\rm el}$ can be fitted to

$$T_{\rm el}(t, E_0) = T_{\rm el}^i(E_0)e^{-t/\tau_{\rm el}} + T_{\rm el}^f(E_0)(1 - e^{-t/\tau_{\rm el}}). \tag{25}$$

Our MFD suggests $\tau_{\rm el} \approx 10\tau_0$, while the ratio $T_{\rm el}^f/T_{\rm el}^i$ is E_0 independent and $T_{\rm el}^f$ can be calibrated from E_0 (Appendix A). We set the rest of the parameters $t_{\rm hop} = 1$, $g = 2$, $M = 25$, $K = 1$, $\tau_0 = 2\pi/\sqrt{K/M}$, $E_p = g^2/2K$. $\gamma = 0.05$, $T_{\rm ph}/t_{\rm hop} = 10^{-3}$. $T_{\rm el}^f$ is varied keeping $T_{\rm el}^i/T_{\rm el}^f = 1.1$. We study $L \times L$ geometry with $L = 30,\ 40,\ 60,\ 80,\ 100$.

D. Results on order-parameter loss-recovery dynamics

Our investigation of this classical model reveals three distinct regimes dependent on $T_{\rm el}^f$, akin to the findings in MFD. $T_{\rm el}^f \lesssim 0.3E_p$ induce oscillations in $x_{\mathbf{Q}}(t)$, similar to ringing. These oscillations dampen over time mainly due to the phenomenological damping γ, with a timescale proportional to $\tau_w \sim 1/\gamma$. Similarly, for $T_{\rm el}^f > 0.45E_p$ no recovery occurs.

We focus in Fig. 12 on the critical dynamics window. In Fig. 12(a), we observe the loss and recovery dynamics in $|x_{\mathbf{Q}}(t)|$. As $T_{\rm el}^f \to 0.455E_p$, which we label $T_{\rm el}^c$, a transition becomes evident. We fit the recovery part of $|x_{\mathbf{Q}}(t)|$ with $|x_{\mathbf{Q}}(t)| \sim X_0\, e^{-(\tau_r/t)^\beta}$ where $X_0 = |x_{\mathbf{Q}}(\infty)|$ and β ranging from 4–6. In Fig. 12(b), we depict the dependence of $|x_{\mathbf{Q}}(\infty)|$ and τ_r on $T_{\rm el}^f$. The recovered amplitude $|x_{\mathbf{Q}}(\infty)|$ behaves like $\sim|T_{\rm el}^f - T_{\rm el}^c|^\alpha$, with $\alpha = 0.62$. The recovery time is fitted to $\tau_r \sim |T_{\rm el}^f - T_{\rm el}^c|^{-\nu}$ with $\nu = 0.31$.

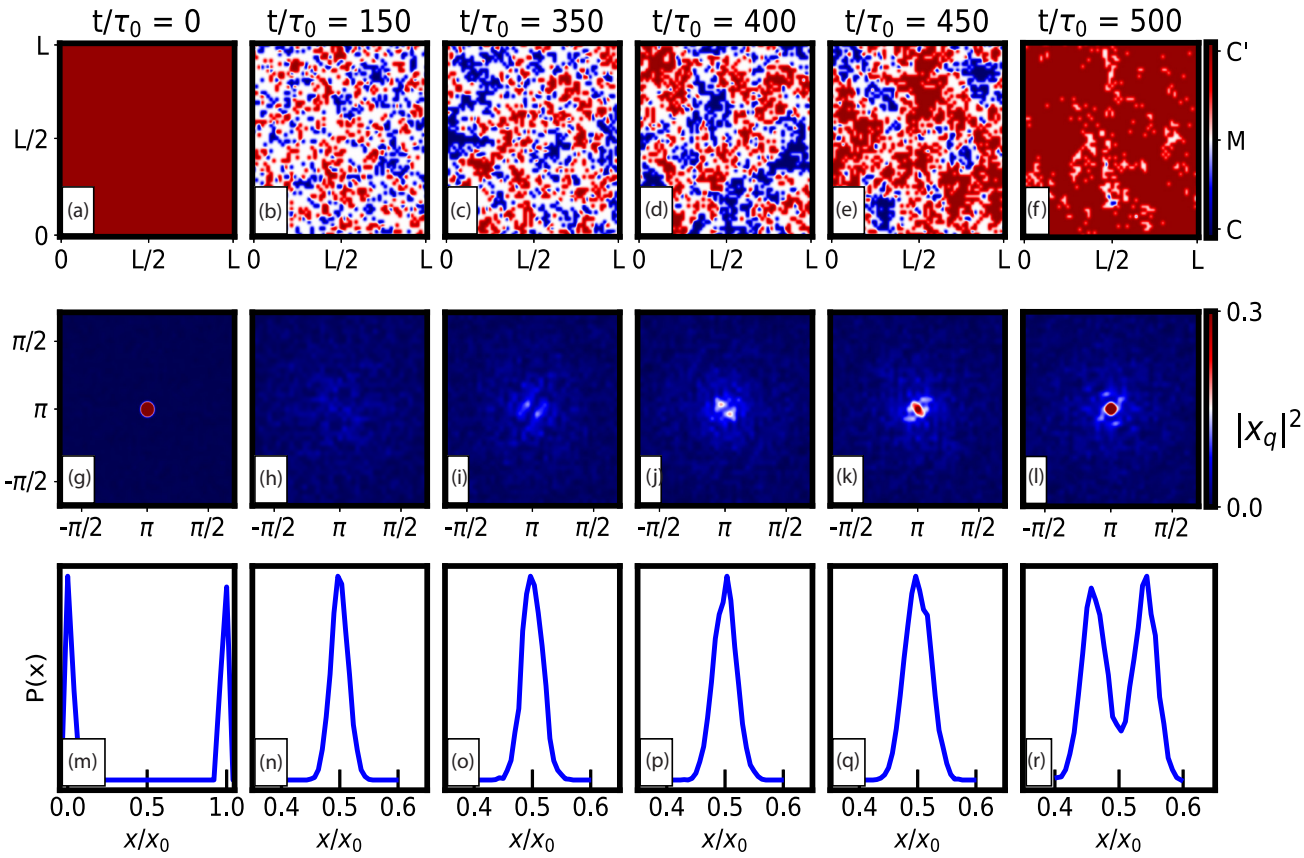

FIG. 13. Suppression and revival dynamics in the 2D classical model with $T_{\rm el}^f = 0.45E_p$ on a 60×60 lattice. The top row shows charge-order domains (see text). Red represents the C-type checkerboard pattern, blue denotes the phase-shifted state C', while white indicates no modulations, referred to as the M state. At $t = 0$, a perfect C state exists, disrupted by the pump over time. At approximately $150\tau_0$, equal amounts of red, white, and blue domains emerge. Around $350\tau_0$, blue and red domains start to cluster, reducing the M state, leading to a CO state C by $500\tau_0$. The middle panel shows $|x_{\mathbf{q}}|^2$ with the suppression and recovery of the (π, π) peak with time. The bottom row displays time dependence of the $P(x)$ distribution. The sharp bimodal feature at $t = 0$ homogenizes by $150\tau_0$. This persists to $300\tau_0$, before a broadened distribution reemerges around $350\tau_0$. At $500\tau_0$, the long-time distribution appears with a much smaller modulation in x compared to $t = 0$.

Figure 13, top panel, illustrates the real-space dynamics of domain formation and growth in a system sized 60×60 with $T_{\rm el}^f = 0.45E_p$. In equilibrium, lattice distortions exhibit a modulation of approximately $\sim g/2K$ around the mean distortion, which is also $\sim g/2K$. By subtracting the average distortion $g/2K$ at each site and multiplying by a periodic modulation $e^{i\mathbf{Q}\cdot\vec{r}_i}$, we homogenize the periodic structure to a positive (C-state) or negative (C'-state) uniform field in the perfectly charge-ordered (CO) background. In the absence of a background CO structure, the amplitude is zero: we term it the M state. Following the pump, the initial C state diminishes, and around $t \sim 150\tau_0$, equal amounts of C, C', and M type exist in a short-range correlated manner. By $t \sim 350\tau_0$, the C and C' states begin to dominate, and a domain competition ensues with C eventually prevailing around $t \sim 450\tau_0$. The middle panel depicts the structure factor $|x_{\mathbf{q}}|^2$, reflecting the loss and recovery of weight at $\mathbf{q} = \mathbf{Q}$. The bottom row shows the time dependence of the $P(x)$ distribution. The sharp bimodal feature at $t = 0$ homogenizes by $150\tau_0$ and persists until $300\tau_0$, before a broadened distribution reemerges around $350\tau_0$. By $500\tau_0$, a "long-time" distribution emerges with a much smaller modulation in x compared to $t = 0$.

Not just the critical dynamics, but the different dynamical regimes are also present in this phenomenological model. In the next section we discuss those regimes.

E. Identification of three regimes from the classical model

As a result of increasing $T_{\rm el}^f$ the $x_{\mathbf{Q}}(t)$ in 2D shows dynamical regimes similar to what is observed in MFD, i.e., WOS, SSR, MS as shown in Fig. 14. Remarkably, these have an analog in the dynamics of $x_-(t)$ in the simple two-site problem. We examine the energetics of the two-site model first, in response to an increase in $T_{\rm el}$, and then move to the lattice model.

In the two-site setup, the key variable is $x_- = x_1 - x_2$, a crude mimic of $x_{\mathbf{Q}}$ on the lattice. We denote x_- by y in what follows. The effective potential $V_{\rm eff}(y)$, depicted in Fig. 11, reveals a double-well structure with prepulse minima at $\pm y_{\rm min}(T_{\rm el} = 0)$. An abrupt increase in $T_{\rm el}$ alters the minima locations to a suppressed value $\pm y_{\rm min}(T_{\rm el})$, accompanied by a reduction in the "barrier height" $\Delta_b(T_{\rm el})$ between the minima and the maximum. Alteration of the potential makes the original minimum a "high-energy" location now, with an excess

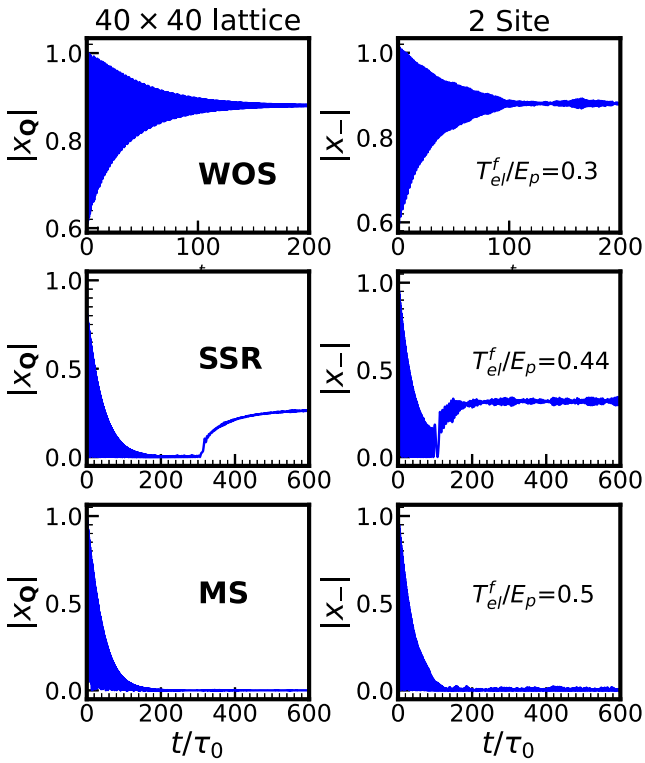

FIG. 14. On the top panels, we observe weak oscillatory suppression (WOS) with $T^f_{\rm el}/E_p = 0.3$ in $x_{\mathbf{Q}}$ on a 40×40 lattice (a). In (b), we observe similar dynamics in x_-. Both are normalized to their equilibrium value. (c), (d) Show strong suppression and recovery (SSR) dynamics at $T_{\rm el}/E_p = 0.44$. While their revival values are the same, their dynamics differ in detail. At $T_{\rm el}/E_p = 0.5$, we observe monotonic suppression (MS) in both the 2D and two-site cases (e), (f).

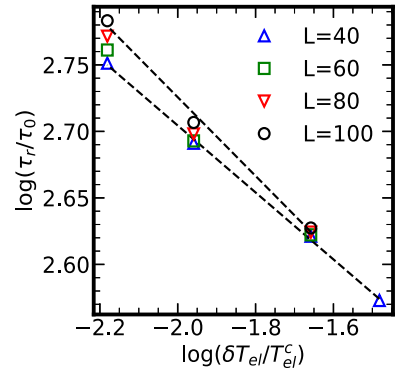

FIG. 15. Log-log plot of the recovery time τ_r vs $\delta T_{\rm el} = |T^f_{\rm el} - T^c_{\rm el}|$ for different system sizes. The difference in recovery time increases with system size faster for small values of $\delta T_{\rm el}$. We plot this for $L = 40, 60, 80, 100$. Dotted lines correspond to linear fittings to $L = 40$ and 100 system sizes.

energy $\mathcal{E}(T^f_{\rm el}) = V(y_{\rm min}(0), T^f_{\rm el}) - V(y_{\rm min}(T^f_{\rm el}), 0) - \Delta\mathcal{E}(T^f_{\rm el})$ where $\Delta\mathcal{E}(T_{\rm el}) = V(0, T^f_{\rm el}) - V(0, 0)$. The two-site problem cannot settle down into its new minimum unless this excess energy is dissipated. We categorize the possibilities as follows:

(i) *Suppressed oscillations*. As $T^f_{\rm el}$ increases from zero, the excess energy $\mathcal{E}(T^f_{\rm el})$ rises while $\Delta_b(T^f_{\rm el})$ begins to decrease. At some $T^f_{\rm el} = T^w_{\rm el}$, say, these values intersect and $\mathcal{E}(T^f_{\rm el}) = \Delta_b(T^f_{\rm el})$. For $T^f_{\rm el} < T^w_{\rm el}$, oscillations in y are confined to a single well within the system. Dissipation causes $\mathcal{E}(T^f_{\rm el})$ to decay as $\sim\mathcal{E}(0)e^{-\gamma t}$, and $y(t)$ stabilizes to the steady-state value $y(T^f_{\rm el})$ over a time scale $\tau_w \sim \frac{1}{\gamma}$.

(ii) *Monotonic suppression*. If $T^f_{\rm el}$ surpasses the critical value $T^c_{\rm el}$ such that $\Delta_b(T^f_{\rm el}) = 0$, no double-well structure exists in $V(y, T^f_{\rm el})$. Then y decays to zero with a timescale $\sim\frac{1}{\gamma}$.

(iii) *Loss and recovery*. In the intermediate window, where $T^w_{\rm el} \leqslant T^f_{\rm el} \leqslant T^c_{\rm el}$, despite the presence of a double well in $V(y, T^f_{\rm el})$, the excess energy is large enough to allow y oscillating between wells. y can "condense" into one of the wells of $V(y, T^f_{\rm el})$ when $\mathcal{E}(t = \tau_r, T^f_{\rm el}) = \Delta_b(T^f_{\rm el})$. Roughly, $\tau_r = \frac{1}{\gamma}\ln[\mathcal{E}(T^f_{\rm el})/\Delta_b(T^f_{\rm el})] \sim F(T^f_{\rm el}) - \frac{1}{\gamma}\ln[\Delta_b(T^f_{\rm el})]$. Here, $F(T^f_{\rm el})$ is noncritical. This growth of the recovery timescale is a feature of purely "local" physics. A more complicated variant of this takes place on the lattice. On the whole this analysis shows how three regimes can arise due to changes in $T_{\rm el}$ even in a two-site problem as shown in Fig. 14.

On the lattice these regimes are also present and the corresponding $T_{\rm el}$ values match at regime boundaries. For WOS and MS we see similar dynamics in $x_{\mathbf{Q}}$ as shown in Fig. 14. On the lattice, however, the relaxation toward the steady state in the SSR regime now includes both amplitude growth and spatial organization. These are intertwined as visible in the width of the distribution $P(x)$. To analyze this, in Fig. 15, we plot the recovery time τ_r against $\delta T_{\rm el} = |T^f_{\rm el} - T^c_{\rm el}|$ for various system sizes $L = 40,\ 60,\ 80,\ 100$. The recovery time increases more rapidly at larger size, particularly pronounced for $T^f_{\rm el}$ in the critical regime.

VI. DISCUSSION

A. Size effects in MFD: Locating the critical point

The MFD computation time scales as $N^2 N_\tau$, where N is the number of lattice sites and N_τ is the number of integration time steps in the interval $[0 - \tau_{\rm max}]$. Within resource limits, we could access $N \sim 400$ and $N_\tau \sim 10^6$ (involving about 10^4–10^5 phonon oscillations). While this was adequate in the weak and strong pulse regimes, accessing the critical regime, where the recovery time τ_{cr} diverges as $E_0 \to E^c_0$, was difficult. We had to extract the $t \to \infty$ value of $x_{\mathbf{Q}}$ by fitting. Figure 16 shows the result of $x_{\mathbf{Q}}(t \to \infty)$ as a function of E_0 for different L.

We fit $|x_{\mathbf{Q}}|^2$ to $|E_0 - E^c_0|^\alpha$, which suggests $E^c_0 \sim 0.48$ with $\alpha = 0.7$. Similarly, τ_r demonstrates a good fit with $|E_0 - E^c_0|^{-\nu}$, where $\nu \sim 0.45$. However, due to the size limitations of our simulations, we must acknowledge that these exponents are not definitive. We have done our best to fit the data to our current knowledge, but larger system sizes would be required to precisely determine the critical exponents.

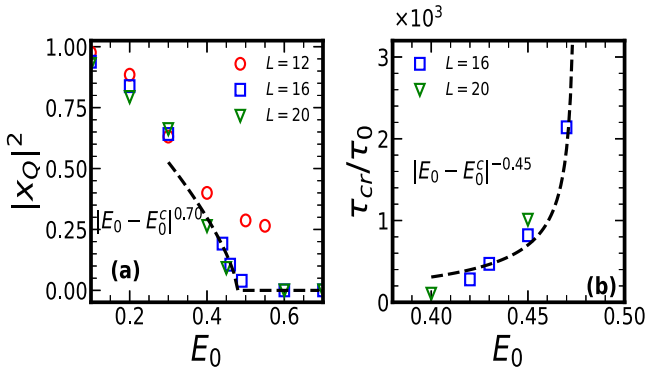

FIG. 16. We show (a) $|x_{\mathbf{Q}}|^2$ and (b) recovery time $\tau_{\rm cr}$ (b) obtained from MFD for various system sizes. Fitting $|x_{\mathbf{Q}}|^2$ to $|E_0 - E_0^c|^\alpha$ suggests a critical value $E_0^c \sim 0.48$ with $\alpha = 0.7$. For a given $\tau_{\rm max}$, capturing τ_r for larger systems ($L = 20$) proves challenging, while for $L = 12$, the system exhibits unclear loss-recovery dynamics. Notably, for $L = 16$, $\tau_{\rm cr}$ demonstrates a good fit with $|E_0 - E_0^c|^{-\nu}$, where $\nu \sim 0.45$.

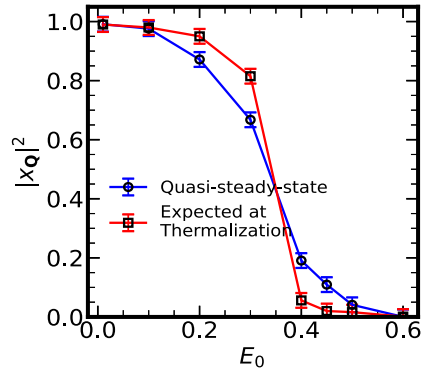

FIG. 17. Associated with the laser pulse amplitude E_0 we calculate the excess energy $\Delta\mathcal{E}$ and compare the structure factor $|x_{\mathbf{Q}}|^2$ at steady state (blue) with the system with same $\Delta\mathcal{E}$ at thermal equilibrium (red). This suggests if the system was able to redistribute its excess energy and reach an internal thermalization, the structure factor would be similar though the nature of the suppression would change from amplitude driven to fluctuation driven.

B. Thermalization

Mean field treatment of a photopumped system often cannot capture the eventual thermalization, the effective electron and phonon temperatures remain different. To that extent one could ask what is the relevance of the long-time state that emerges in our calculations. There are two aspects we briefly comment on: (i) an estimate of the thermalization time based on work that has been done on other gapped systems, and (ii) the comparison of the state that we obtain at a pump intensity E_0, and associated excess energy $\Delta\mathcal{E}$, with the equilibrium state that would have resulted if the system had excess *thermal energy*$\Delta\mathcal{E}$.

Regarding thermalization, time-specific calculations have been done on Mott insulators. The conclusion there is that a pump pulse excites electrons across the gap Δ, creating double occupancy, and these electrons deexcite by multimagnon emission, each magnon having an energy $\sim J = 4t^2/U$, where U is the Hubbard repulsion. An early estimate of the decay time was provided by Strohmaier *et al.* [54] who suggest a result of the form $\tau_D \sim \frac{\hbar}{J} e^{(\alpha \frac{U}{zJ})}$, where z is the coordination number of the lattice. The coefficient $\alpha \sim O(1)$. The essence of this result is that the time for emitting multiple bosons, each of energy $\sim zJ$, to dexcite an electron at at energy $U \gg zJ$ is exponentially large. The emission processes have to act in sequence. This was established through an exact diagonalization calculation by Lenarcic and Prelovsek [55]. We are not aware of an equivalent calculation for the Holstein model but the physical process invoked in the Mott insulator suggests that electrons excited across the charge ordering gap $\Delta_{\rm CO}$ would deexcite by emitting phonons with energy $\sim\hbar\Omega_0$. In our problem the gap is $\Delta_{\rm CO} \sim 1.5t_{\rm hop}$ and the phonon frequency is $\sim\hbar\Omega_0 = 0.2t_{\rm hop}$. Even with intersite coupling the phonons have a narrow band of energies around $\hbar\Omega_0$. As a result, following, Strohmaier *et al.*, we expect $\tau_D \sim \tau_0 \exp(\frac{\Delta_{\rm CO}}{\hbar\Omega_0})$. At our parameter point this is $\sim 1800\tau_0$. So, in a fuller calculation we expect that the intermediate time dynamics that we see, on the scale of few hundred τ_0, would remain, but at longer times the upper band population will relax leading to a common temperature for phonons and electrons. Our "divergent" timescale would be cut off.

We can compare the long-time state, characterized by an added energy $\Delta\mathcal{E}(E_0)$, with what arises in an equilibrium thermal situation witn the same energy $\Delta\mathcal{E}(T)$. The equilibrium excess energy $\Delta\mathcal{E}(T) = \mathcal{E}(T) - \mathcal{E}(0)$ can be worked out from Monte Carlo or Langevin calculation on the electron-phonon system. Once the map from E_0 to T is obtained we can compare the order parameter in the long-time pumped state with a thermal state at the same excess energy. The comparison is in Fig. 17. While the critical E_0 estimate is reasonable, the actual thermal transition and the pump-drive transition have the following difference. The suppression in $|x_{\mathbf{Q}}|^2$ in the photopump case is due to the amplitude suppression but the suppression in $|x_{\mathbf{Q}}|^2$ in thermal case is more Ising type, where the x_i amplitude distribution remains roughly similar at zero and finite temperature but interference between domains leads to loss of long-range order.

VII. CONCLUSIONS

We have studied the effect of a short laser pulse on a charge-ordered system, realized in the two-dimensional half-filled spinless Holstein model. We work at intermediate electron-phonon coupling, roughly ∼40% of the coupling needed for a single-polaron formation, and study the coupled dynamics of the lattice variables (x_i) and the electronic correlator $\rho_{ij}(t) = \langle c_i^\dagger(t) c_j(t)\rangle$ within a mean field dynamics scheme. The method is nonperturbative in electron-phonon coupling and handles spatial correlations exactly. The dynamics can be categorized into three regimes with increasing pulse strength. At weak pulse strength we find a small oscillatory suppression of the order parameter to a finite long-time value. At intermediate pulse strength (which we label as the critical regime) the dynamics show strong suppression and revival of the order parameter. This involves a rapid drop of the order parameter to almost zero, where the system stays for a time

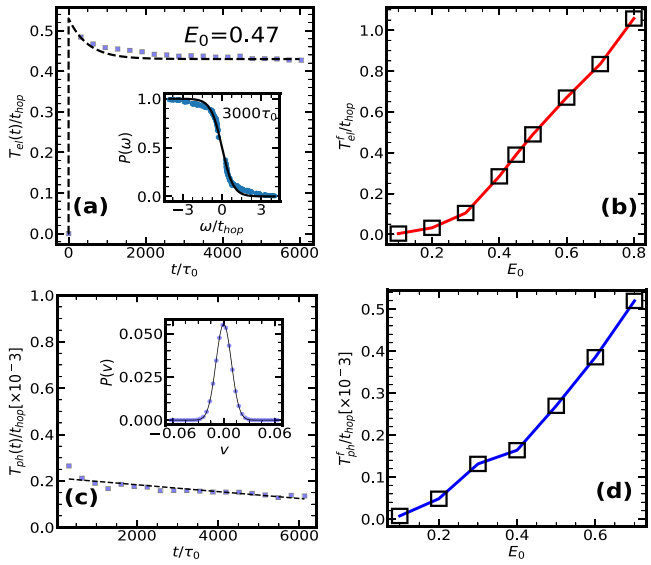

FIG. 18. Top panels: Extracting an "electronic temperature": (a) The population function $f(\omega)$ obtained from MFD is fitted to a Fermi function with $T_{\rm el}(t)$. $T_{\rm el}(t)$ settles down to a value $T_{\rm el}^f$ over a timescale $\tau_{\rm el}$; the exponential fit is shown. The inset shows the Fermi function fit to $f(\omega)$ at some t. (b) The long-time value of $T_{\rm el}^f$ for varying E_0. Bottom panels: Extracting a "phonon temperature." (c) The speed distribution $P(v)$ obtained from MFD is fitted to a Maxwell-Boltzmann function with temperature $T_{\rm ph}(t)$. $T_{\rm ph}$ is almost constant with time. The inset shows the distribution function fit. (d) The long-time value of $T_{\rm ph}$ for varying E_0.

$\sim\tau_{\rm cr}$, and then a power law rises to a finite long-time value. We find that $\tau_{\rm cr} \to \infty$ and the long-time value $\to 0$, as the pulse strength E_0 tends to a critical value E_0^c. This defines a nonequilibrium phase transition. We have established the transition by studying the system on accessible lattice size (up to 20×20) and time windows. For a strong pulse, the CO order parameter decays monotonically to zero. Associated with the CO order-parameter behavior is a gap-closing and -reopening transition in the critical regime and a gap closing transition in the strong pulse regime. Since full mean field dynamics is expensive on large lattices we constructed an effective classical model for the phonons where the phonon dynamics is driven by a nonequilibrium electron population derived from MFD. This model captures all the three regimes that one sees in MFD and provides better access to critical properties than MFD does. Both MFD and the classical model suffer from lack of equilibration between electrons and phonons and our results would be modified when these "beyond mean field" effects are incorporated. We provide an estimate of this timescale.

ACKNOWLEDGMENT

We acknowledge the use of the HPC clusters at HRI.

APPENDIX A: ELECTRON AND PHONON TEMPERATURES, AND DISSIPATION RATE

Estimation of T_{el} and T_{ph}. From the MFD we can track the excited population $n_{\rm exc}(t, E_0)$ and map it to a $T_{\rm el}(t, E_0)$. Figure 18(a) shows such a time-dependent profile for $T_{\rm el}$ and the inset shows a long-time distribution function that is fitted by a Fermi function. The time dependence of $T_{\rm el}$ can be fitted to

$$T_{\rm el}(t, E_0) = T_{\rm el}^i e^{-t/\tau_{\rm el}} + T_{\rm el}^f(E_0)(1 - e^{-t/\tau_{\rm el}}) \tag{A1}$$

our MFD suggests $\tau_{\rm el} \approx 10\tau_0$, while $T_{\rm el}^f$ depends on E_0 in the manner shown in Fig. 18(b). Similarly from the distribution of the momentum p_i, an estimation of phonon temperature can be made by fitting the time-dependent distribution to Maxwell-Boltzmann distribution as shown in Fig. 18(c). The time dependence of the $T_{\rm ph}(t)$ is also shown which remains almost constant for the most of the simulation time. Its E_0 dependence is in Fig. 18(d). It should be noticed that $T_{\rm el}^f$ is $\sim 10^3$ larger than $T_{\rm ph}$.

Estimation of dissipation rate γ. The equation for oscillator in MFD is $M\frac{d^2x_i}{dt^2} = -Kx_i + g\rho_{ii}$. This onsite density ρ_{ii} can be written as the instantaneous term (calculated from the phonon background with electronic population) and its fluctuation as $\rho_{ii} = n_i^{\rm inst} + \delta n_i(t)$. We assume this fluctuation to be of form $g\delta n_i(t) = -\gamma\frac{dx_i}{dt} + \eta_i(t)$. At large frequency $|\delta n_i(\omega)|^2$ only contributes to $|\eta_i(\omega)|^2$ which is a constant $\frac{2}{g^2}\gamma T_{\rm ph}$. From this we get an estimate for $\gamma T_{\rm ph} \sim 10^{-5} t_{\rm hop}$ at $E_0 \sim 0.4$. Our estimate of $T_{\rm ph}/t_{\rm hop}$ is between 10^{-3} to 10^{-4}. So, our estimate for γ is of order 10^{-2} to 10^{-1}.

APPENDIX B: GINZBURG-LANDAU MODEL IN THE CRITICAL REGIME

It is usual to write a phenomenological Ginzburg-Landau (GL) model based on order-parameter symmetry to capture the essential physics when the amplitude of the ordering field is small. To connect to these kinds of work in the literature we derive an explicit lattice GL model, expanded to fourth order in the scalar field ξ_i, with nearest-neighbor "antiferro" coupling between sites to promote a modulated state. The energy function below has three parameters, A, B, C, which can be derived explicitly from the Holstein energy functional, retaining the effect of $T_{\rm el}$, $\xi_i = x_i - x_{\rm av}$,

$$V(\xi) = \sum_i \left(A\xi_i^2 + B\xi_i^4\right) + C\sum_{ij}\xi_i\xi_j \tag{B1}$$

and higher-order intersite terms. Here,

$$A(T_{\rm el}) = \frac{1}{2}\left(K - \frac{g^2}{4t_{\rm hop}}\tanh\left[\frac{t_{\rm hop}}{T_{\rm el}}\right]\right), \tag{B2}$$

$$B(T_{\rm el}) = \frac{g^4}{32t_{\rm hop}^3}\left(\tanh\left[\frac{t_{\rm hop}}{T_{\rm el}}\right] - \frac{t_{\rm hop}}{T_{\rm el}}\,{\rm sech}^2\left[\frac{t_{\rm hop}}{T_{\rm el}}\right]\right), \tag{B3}$$

$$C(T_{\rm el}) = \frac{g^2}{8t_{\rm hop}}\tanh\left[\frac{t_{\rm hop}}{T_{\rm el}}\right]. \tag{B4}$$

For actual dynamics, the equation of motion will involve thermal noise and a dissipation

$$M\frac{d^2\xi_i}{dt^2} = -\frac{\partial V}{\partial\xi_i} - \gamma\frac{d\xi_i}{dt} + \eta_i, \tag{B5}$$

where the dissipation coefficient γ and the strength of the noise η satisfy the fluctuation-dissipation theorem.

[1] J. Bloch, A. Cavalleri, V. Galitski, M. Hafezi, and A. Rubio, Nature (London) **606**, 41 (2022).

[2] E. Beaurepaire, J.-C. Merle, A. Daunois, and J.-Y. Bigot, Phys. Rev. Lett. **76**, 4250 (1996).

[3] E. Carpene, E. Mancini, C. Dallera, M. Brenna, E. Puppin, and S. De Silvestri, Phys. Rev. B **78**, 174422 (2008).

[4] P. Beaud, S. L. Johnson, E. Vorobeva, U. Staub, R. A. De Souza, C. J. Milne, Q. X. Jia, and G. Ingold, Phys. Rev. Lett. **103**, 155702 (2009).

[5] M. Fiebig, K. Miyano, Y. Tomioka *et al.*, Appl. Phys. B **71**, 211 (2000).

[6] H. Matsuzaki, H. Uemura, M. Matsubara, T. Kimura, Y. Tokura, and H. Okamoto, Phys. Rev. B **79**, 235131 (2009).

[7] M. Chávez-Cervantes, G. E. Topp, S. Aeschlimann, R. Krause, S. A. Sato, M. A. Sentef, and I. Gierz, Phys. Rev. Lett. **123**, 036405 (2019).

[8] S. Iwai, M. Ono, A. Maeda, H. Matsuzaki, H. Kishida, H. Okamoto, and Y. Tokura, Phys. Rev. Lett. **91**, 057401 (2003).

[9] H. Okamoto, H. Matsuzaki, T. Wakabayashi, Y. Takahashi, and T. Hasegawa, Phys. Rev. Lett. **98**, 037401 (2007).

[10] D. Cho, S. Cheon, K. Kim, S. H. Lee, Y. H. Cho, S. W. Cheong, and H. W. Yeom, Nat. Commun. **7**, 10453 (2015).

[11] H. Ichikawa, S. Nozawa, T. Sato *et al.*, Nat. Mater. **10**, 101 (2011).

[12] Q. M. Liu, D. Wu, Z. A. Li *et al.*, Nat. Commun. **12**, 2050 (2021).

[13] M. Budden, T. Gebert, M. Buzzi *et al.*, Nat. Phys. **17**, 611 (2021).

[14] D. Fausti, R. I. Tobey, N. Dean, S. Kaiser, A. Dienst, M. C. Hoffmann, S. Pyon, T. Takayama, H. Takagi, and A. Cavalleri, Science **331**, 189 (2011).

[15] Y. Zhang, X. Shi, W. You, Z. Tao, Y. Zhong, F. Kabeer, P. Maldonado, P. Oppeneer, M. Bauer, K. Rossnagel, H. Kapteyn, and M. Murnane, Proc. Natl. Acad. Sci. USA **117**, 8788 (2020).

[16] J. Maklar, Y. W. Windsor, C. W. Nicholson *et al.*, Nat. Commun. **12**, 2499 (2021).

[17] F. Schmitt, P. Kirchmann, U. Bovensiepen, R. Moore, J. Chu, D. Lu, L. Rettig, M. Wolf, I. Fisher, and Z. Shen, New J. Phys. **13**, 063022 (2011).

[18] L. Rettig, S. O. Mariager, A. Ferrer, S. Grübel, J. A. Johnson, J. Rittmann, T. Wolf, S. L. Johnson, G. Ingold, P. Beaud, U. Staub, Phys. Rev. Lett. **114**, 067402 (2015).

[19] T. Han, F. Zhou, C. Malliakas, P. Duxbury, S. Mahanti, M. Kanatzidis, and C.-Y. Ruan, Sci. Adv. **1**, e1400173 (2015).

[20] S. Hellmann, M. Beye, C. Sohrt, T. Rohwer, F. Sorgenfrei, H. Redlin, M. Kallane, M. Marczynski-Buhlow, F. Hennies, M. Bauer, A. Fohlisch, L. Kipp, W. Wurth, and K. Rossnagel, Phys. Rev. Lett. **105**, 187401 (2010).

[21] E. Carpene, E. Mancini, C. Dallera, G. Ghiringhelli, C. Manzoni, G. Cerullo, and S. D. Silvestri, Rev. Sci. Instrum. **80**, 055101 (2009).

[22] J. A. Sobota, Y. He, and Z.-X. Shen, Rev. Mod. Phys. **93**, 025006 (2021).

[23] S. Eich, A. Stange, A. Carr, J. Urbancic, T. Popmintchev, M. Wiesenmayer, K. Jansen, A. Ruffing, S. Jakobs, T. Rohwer, S. Hellmann, C. Chen, P. Matyba, L. Kipp, K. Rossnagel, M. Bauer, M. Murnane, H. Kapteyn, S. Mathias, and M. Aeschlimann, J. Electron Spectrosc. Relat. Phenom. **195**, 231 (2014).

[24] N. Gedik and I. Vishik, Nat. Phys **13**, 1029 (2017).

[25] C. Jia, K. Wohlfeld, Y. Wang, B. Moritz, and T. P. Devereaux, Phys. Rev. X **6**, 021020 (2016).

[26] M. Mitrano and Y. Wang, Commun Phys **3**, 184 (2020).

[27] M. Rechtsman, J. Zeuner, Y. Plotnik *et al.*, Nature (London) **496**, 196 (2013).

[28] T. Oka and S. Kitamura, Annu. Rev. Condens. Matter Phys. **10**, 387 (2019).

[29] M. Bukov, L. D'Alessio, and A. Polkovnikov, Adv. Phys. **64**, 139 (2015).

[30] H. Fröhlich, Adv. Phys. **3**, 325 (1954).

[31] E. K. H. Salje, A. S. Alexandrov, and W. Y. Liang, *Polarons and Bipolarons in High Temperature Superconductors and Related Materials* (Cambridge University Press, Cambridge, 1995).

[32] C. Franchini, M. Reticcioli, M. Setvin *et al.*, Nat. Rev. Mater. **6**, 560 (2021).

[33] C. P. Adams, J. W. Lynn, Y. M. Mukovskii, A. A. Arsenov, and D. A. Shulyatev, Phys. Rev. Lett. **85**, 3954 (2000).

[34] O. Bradley, G. G. Batrouni, and R. T. Scalettar, Phys. Rev. B **103**, 235104 (2021).

[35] R. H. McKenzie, C. J. Hamer, and D. W. Murray, Phys. Rev. B **53**, 9676 (1996).

[36] S. Pradhan and G. V. Pai, Phys. Rev. B **92**, 165124 (2015).

[37] C. W. Chen, J. Choe, and E. Morosan, Rep. Prog. Phys. **79**, 084505 (2016).

[38] N. C. Costa, K. Seki, S. Yunoki, and S. Sorella, Commun. Phys. **3**, 80 (2020).

[39] A. Vernes and P. Weinberger, Phys. Rev. B **71**, 165108 (2005).

[40] J. Bünemann and G. Seibold, Phys. Rev. B **96**, 245139 (2017).

[41] J. K. Freericks, H. R. Krishnamurthy, and T. Pruschke, Phys. Rev. Lett. **102**, 136401 (2009).

[42] M. Eckstein and M. Kollar, Phys. Rev. B **78**, 245113 (2008).

[43] G. Khitrova, P. R. Berman, and M. Sargent, J. Opt. Soc. Am. B **5**, 160 (1988).

[44] P. E. Dolgirev, A. V. Rozhkov, A. Zong, A. Kogar, N. Gedik, and B. V. Fine, Phys. Rev. B **101**, 054203 (2020).

[45] P. E. Dolgirev, M. H. Michael, A. Zong, N. Gedik, and E. Demler, Phys. Rev. B **101**, 174306 (2020).

[46] J. Okamoto, New J. Phys. **21**, 123040 (2019).

[47] B. Moritz, T. P. Devereaux, and J. K. Freericks, Phys. Rev. B **81**, 165112 (2010).

[48] O. P. Matveev, A. M. Shvaika, T. P. Devereaux, and J. K. Freericks, Phys. Rev. B **94**, 115167 (2016).

[49] M. D. Petrovic, M. Weber, and J. K. Freericks, arXiv:2203.11880.

[50] M. Weber and J. K. Freericks, Phys. Rev. E **105**, 025301 (2022).

[51] J. Luo and G. W. Chern, Phys. Rev. B **103**, 115137 (2021).

[52] S. Bhattacharyya, S. S. Bakshi, S. Pradhan, and P. Majumdar, Phys. Rev. B **101**, 125130 (2020).

[53] S. Bhattacharyya, S. S. Bakshi, S. Kadge, and P. Majumdar, Phys. Rev. B **99**, 165150 (2019).

[54] N. Strohmaier, D. Greif, R. Jördens, L. Tarruell, H. Moritz, T. Esslinger, R. Sensarma, D. Pekker, E. Altman, and E. Demler, Phys. Rev. Lett. **104**, 080401 (2010).

[55] Z. Lenarčič and P. Prelovšek, Phys. Rev. Lett. **111**, 016401 (2013).